arXiv:0706.4330v1 [astro-ph] 28 Jun 2007

ApJ, accepted

Molecular Outflows and a Mid-Infrared Census of the Massive Star-Formation Region Associated with IRAS 18507+0121

D. S. Shepherd[1,2], M. S. Povich[3], B. A. Whitney[4], T. P. Robitaille[5], D. E. A. Nürnberger[6], L. Bronfman[7], D. P. Stark[8], R. Indebetouw[9], M. R. Meade[3], & B. L. Babler[3]

ABSTRACT

We have observed the central region of the IR-dark cloud filament associated with IRAS 18507+0121 at millimeter wavelengths in CO(J=1−0), ^{13}CO(J=1−0), and C^{18}O(J=1−0) line emission and with the *Spitzer Space Telescope* at mid-IR wavelengths. Five massive outflows from two cloud cores were discovered. Three outflows are centered on or near an Ultracompact HII (UC HII) region (G34.4+0.23) while the remaining two outflows originate from the millimeter core G34.4+0.23 MM. Modeling of the SEDs of the mid-IR sources identified 31 young stellar objects in the filament with a combined stellar mass of $\sim 127 \pm 27\,M_\odot$. An additional 22 sources were identified as probable cluster members based on the presence of strong 24 μm emission. The total star formation efficiency in the G34.4 cloud filament is estimated to be $\sim 7\%$ while the massive and intermediate mass star formation efficiency in the entire cloud filament is estimated to be

[1]National Radio Astronomy Laboratory, P.O. Box O, 1003 Lopezville Rd, Socorro, NM 87801.

[2]The National Radio Astronomy Observatory is a facility of the National Science Foundation operated under cooperative agreement by Associated Universities, Inc.

[3]Department of Astronomy, University of Wisconsin at Madison, 475 N. Charter St. Madison, WI 53706

[4]Space Science Institute, 4750 Walnut St. Suite 205, Boulder, CO 80301, bwhitney@spacescience.org.

[5]SUPA, School of Physics and Astronomy, University of St Andrews, North Haugh, KY16 9SS, St Andrews, United Kingdom; tr9@st-andrews.ac.uk.

[6]European Southern Observatory, Casilla 19001, Santiago 19, Chile.

[7]Departamento de Astronomía, Universidad de Chile, Casilla 36-D, Santiago, Chile.

[8]Division of Physics, Mathematics & Astronomy, California Institute of Technology, MS 105-24, Pasadena, CA 91125.

[9]Department of Astronomy, University of Virginia, Charlottesville, VA 22903-0818.

roughly 2%. A comparison of the gravitational binding energy with the outflow kinetic energy suggests that the compact core containing G34.4+0.23 MM is being destroyed by its molecular outflows whereas the outflows associated with more massive core surrounding the G34.4 UC HII region are not likely to totally disrupt the cloud. Additionally, a qualitative evaluation of the region appears to suggest that stars in this region may have formed in two stages: first lower mass stars formed and then, a few Myrs later, the more massive stars began to form.

Subject headings: stars: formation – nebulae: HII regions – ISM: molecules

1. INTRODUCTION

The massive star forming region associated with IRAS 18507+0121 (hereafter IRAS 18507) is located in an infrared dark cloud that was mapped by Rathborne et al. (2005) in millimeter and submillimeter continuum and compared to Spitzer mid-IR emission between 3.5 and 8μm. IRAS 18507 is roughly 11$'$ north of the more famous ultra-compact (UC) HII region complex G34.26+0.15 (Wood & Churchwell 1989; Molinari et al. 1996; Carral & Welch 1992). The location of the infrared dark cloud relative to G34.26+0.15 is shown in Figure 1.

Near IRAS 18507, Miralles et al. (1994) discovered a UC HII region (G34.4+0.23) embedded in a 1000 $M_\odot$ molecular cloud traced by NH_3 emission. The NH_3 emission is elongated in the N-S direction with a total extent of about 7$'$, however the 1.5$'$ resolution of the observations was not adequate to discern the structure of the core (Miralles et al. 1994). Shepherd et al. (2004: hereafter SNB04) observed IRAS 18507 in 3 mm continuum emission, $H^{13}CO^+$ and SiO line emission and in the near-infrared. They detected a dense molecular core associated with the UC HII region G34.4+0.23 as well as a dense core and embedded protostellar object detected only in millimeter continuum emission, G34.4+0.23 MM (hereafter G34.4 MM). G34.4 MM appears to be a B2 protostar surrounded by $\sim$ 150 solar masses of warm gas and dust. Based on the non-detection of G34.4 MM at near-IR wavelengths, SNB04 suggested the source may be in a very early stage of evolution.

Rathborne et al. (2005) identified four clumps in 1.2 mm continuum emission which they named MM1-4 (see their figure 1). MM1 corresponds to G34.4 MM, MM2 is coincident with the UC HII region G34.4+0.23, MM3 is about 3$'$ north of G34.4 MM while MM4 is about 30$''$ south of the UC HII region.

IRAS 18507 was detected in a CS(2-1) survey of IRAS point sources with far-infrared colors suggestive of UC HII regions (Bronfman et al. 1996). The source was selected for further high resolution studies because of its broad line wings, a signature of current star

formation. By modeling HCO^+, $H^{13}CO^+$, CS and $C^{34}S$ spectra obtained at an angular resolution of $\sim 16''$ Ramesh et al. (1997) demonstrated that the observed line profiles can be explained by a collapsing hot core of about $800\,M_\odot$ which is hidden behind a cold ($\sim 4\,K$) and dense ($3 \times 10^4\,cm^{-3}$) envelope of about $200\,M_\odot$.

The kinematic distance to IRAS 18507 has been reported to be between 3.7 and 3.9 kpc based on molecular line velocities that vary from 55 to $59\,km\,s^{-1}$ depending on the line observed and the position within the cloud (3.9 kpc: Molinari et al. 1996, Shepherd et al. 2004, Zhang et al. 2005; 3.8 kpc: Carral & Welch 1992, Miralles et al. 1994, Ramesh et al. 1997; & 3.7 kpc: Rathborne et al. 2005). Kinematic distances can easily have an error of more than 5 or even 10% due to observed deviations from circular symmetry and circular motion in our galaxy. Thus, a difference of 0.2 kpc is easily within the errors for this type of distance determination. Here we adopt the distance of 3.9 kpc to be consistent with Molinari et al. (1996, 1998), SNB04 and Zhang et al. (2005). If the closer distance of 3.7 kpc is more appropriate, then mass estimates derived in this work should be decreased by about 10% since the mass is proportional to D^2.

Faúndez et al (2004) mapped the IR-dark cloud with the SEST telescope in 1.2 mm continuum emission and derived mass of $2000\,M_\odot$ in the main condensation based on a dust temperature of 28°K. The total mass of the filament was estimated to be about $3700\,M_\odot$ where $1000\,M_\odot$ is associated with G34.4 MM and $2700\,M_\odot$ is associated with the G34.4 UC HII region (Bronfman, personal communication). Rathborne et al (2005) mapped the dark cloud with the IRAM 30 telescope in 1.2 mm continuum emission and derived a cloud mass of $\sim 7500\,M_\odot$ based on a dust temperature of 34°K, two times more mass than derived by Faúndez et al. In this work, we will assume the temperature and mass estimates of Rathborne et al. since a dust temperature of 34°K would appear to be more representative of massive star forming regions. However, a clear reason for why the derived temperature and, hence, mass estimates differ by such a large amount is not clear.

The IRAS 18507 region is also associated with variable H_2O, CH_3OH and OH maser emission (Scalise et al. 1989; Palla et al. 1991; Schutte et al. 1993; Miralles et al. 1994; Szymczak et al. 2000; Wang et al. 2006; Edris et al. 2007). Molinari et al. (1996, 1998) observed IRAS 18507 (labeled Mol74 in their papers) and estimated a deconvolved size of the UC HII region of 0.7" (0.013 pc at D=3.9 kpc).

Based on observations with the NRAO 12 m telescope, Zhang et al. (2005) report that IRAS 18507 is not associated with molecular outflows. The lack of outflow activity contrasts with the presence of multiple star formation tracers (masers, dense gas, HII regions and millimeter continuum).

In this work, we present observations of the dense molecular gas near IRAS 18507 at millimeter wavelengths in CO(J=1−0), ^{13}CO(J=1−0), and C^{18}O(J=1−0) line emission to map the dense gas morphology and determine if there are massive outflows associated with IRAS 18507. Archive data from the *Spitzer Space Telescope* GLIMPSE survey at mid-IR wavelengths were studied to obtain a census of the massive and intermediate-mass star cluster properties over the entire infrared-dark cloud filament. Section 2 gives an overview of the observations, section 3 presents the results and section 4 discusses implications.

2. OBSERVATIONS

2.1. Observations in the 3 mm band

Simultaneous observations in CO(J=1−0), ^{13}CO(J=1−0) and C^{18}O(J=1−0) lines were made with the Owens Valley Radio Observatory (OVRO) array of six 10.4 m telescopes on 2004 March 27 & 29 and 2004 April 16 & 18. Projected baselines ranging from about 12 to 115 meters provided sensitivity to structures up to about 20″ with $\sim 5''$ resolution. Two fields were observed as a Nyquist-sampled mosaic. The observations were alternated between fields every 9 minutes to assure that the *uv* coverage in each field was similar. The total integration time on each field was approximately 8.8 hours. Cryogenically cooled SIS receivers operating at 4 K produced typical single sideband system temperatures of about 400 K. The gain calibrator was the quasar 1751 + 096 and the passband calibrators were 3C 345, 3C 454.3 and 3C 273. Observations of Uranus provided the flux density calibration scale with an estimated uncertainty of $\sim 15\%$. Calibration was carried out using the Caltech MMA data reduction package (Scoville et al. 1993). Images were produced using the MIRIAD software package (Sault, Teuben, & Wright 1995) and deconvolved with a Maximum Entropy (MEM) algorithm. Data analysis was performed using both the MIRIAD package and the CASA (Common Astronomy Software Applications) package.

The spectral band pass for each line was centered on a velocity of 57.0 km s^{-1}. The CO images have a synthesized beam of $3.83'' \times 3.45''$ (FWHM) at P.A. $-59.7°$, spectral resolution 1.3 km s^{-1} and RMS noise 60 mJy beam^{-1}. The ^{13}CO images have a synthesized beam of $4.04'' \times 3.83''$ (FWHM) at P.A. $-49.9°$, spectral resolution 1.36 km s^{-1} and RMS noise 44.0 mJy beam^{-1}. The C^{18}O images have a synthesized beam of $4.04'' \times 3.83''$ (FWHM) at P.A. $-50.1°$, spectral resolution 0.683 km s^{-1} and RMS noise 56.0 mJy beam^{-1}.

2.2. Spitzer images

Mid-infrared images at 3.6, 4.6, 5.8 and 8.0 μm were obtained using the Infrared Array Camera (IRAC; Fazio et al. 2004) of the *Spitzer Space Telescope* as part of the Galactic Legacy Infrared Mid-Plane Survey Extraordinaire (GLIMPSE; Benjamin et al. 2003). Image mosaics were created by the GLIMPSE pipeline after image artifacts such as cosmic rays, stray light, column pull-down, and banding were removed.[1]. Point sources were extracted from the GLIMPSE images using a modified version of Daophot (Stetson 1987). The astrometric uncertainty for point sources is $\sim 0.3''$. The GLIMPSE 5σ point-source sensitivities are approximately 0.3, 0.3, 1.2, and 0.7 mJy in the four IRAC band passes, respectively. Point source sensitivities were generally higher in areas of bright diffuse background emission. The fluxes of point sources that are detected at $\geq 5\sigma$ twice in one IRAC band or once in each of two bands are entered in the GLIMPSE Point Source Archive. Each Archive entry includes the corresponding J, H, and K_s fluxes from the 2MASS Point Source Catalog (Skrutskie et al. 2006) if that source was detected in 2MASS.

The Multi-band Imaging Photometer for *Spitzer* (MIPS; Rieke et al. 2004) was used to image the entire GLIMPSE survey area at 24 and 70 μm as part of the MIPSGAL survey (Carey et al. 2005). Fluxes at 24 μm for point sources within the G34.4 IR dark cloud were extracted from the frame using the GLIMPSE point-source extractor. The relative uncertainty between two sources in a MIPSGAL image is roughly 0.3 to 0.5 pixels while the absolute positional uncertainty is $\sim 1''$.

3. RESULTS

Figure 1 presents a four-color (3.6, 4.6, 5.8, & 8.0 μm) GLIMPSE image of the G34.4 environment in Galactic coordinates (North points to the upper left corner). The "cometary" UC HII region G34.26+0.15 is located on the right side of the image. An IR-bright nebula extends below the G34.26 UC HII region. The UC HII region contains a cluster of OB stars, the most luminous of which is an O6.5 spectral type (Wood & Churchwell 1989). The nebula is bright in the IRAC bands primarily due to PAH emission features stimulated by UV radiation from the cluster. The subject of this paper is the dark filament in the upper left which is forming early B stars. The mid-IR emission from the UC HII region G34.4+0.23 is significantly less than that of G34.26, as expected due to the lower luminosity of the central source. Figure 2 presents a close-up of the IR-dark filament, now displayed in Equatorial

[1]Details of the data processing can be found at http://www.astro.wisc.edu/glimpse/docs.html

coordinates with North pointing upwards. Along the dark filament, North and South of G34.4, are embedded sources seen predominantly by their 4.5 μm (green) emission. Our OVRO CO mosaic is centered on the southern core near the UC HII region G34.4 and the millimeter core G34.4 MM located $\sim 40''$ north of the UC HII region.

Figure 3 presents the red and blue-shifted emission near G34.4 MM and G34.4 along with a 2 μm K band image from SNB04. Neither the millimeter core nor the UC HII region is visible in the K band image. Both regions show complex high-velocity structure suggesting the presence of multiple outflows.

Figure 4 shows the integrated emission (moment 0) in $C^{18}O$ and ^{13}CO along with the red and blue-shifted ^{13}CO emission. The bottom two panels in figure 4 show moment 1 maps of $C^{18}O$ & ^{13}CO in which the brightness of the color is proportional to the intensity in the moment 0 image. This type of image provides some insight into how the dense cloud structure and kinematics are being affected by the molecular outflows.

Figures 5, 6 & 7 present channels maps of CO, ^{13}CO and $C^{18}O$ emission, respectively.

3.1. Molecular outflows

At least two outflows can be seen emanating from G34.4 MM (labeled A and B in the upper left panel of Fig. 3) while at least three outflows originate from the southern core near the G34.4 UC HII region (labeled C, D and E).

The velocity structure of the outflows from the G34.4 MM region is consistent with a single outflow dominating the red-shifted kinematics (outflow G34.4:A). There is a weak blue-shifted counter flow extending to the NE that can be traced to G34.4 MM. The red-shifted lobe of outflow G34.4:A appears to have little or no associated blue-shifted emission suggesting that it is oriented outside of the plane of the sky (the blue-shifted emission in the red lobe appears to be from the collimated flow G34.4:E coming from the southern region). The full-opening angle of the red-shifted lobe is $\sim 43°$.

Marginal evidence for an outflow perpendicular to outflow G34.4:A is seen in the red and blue-shifted emission clumps along the axis labeled 'B'. No source has been detected at millimeter wavelengths which could drive outflow G34.4:B. The source could be embedded in G34.4 MM and not resolved at the resolution of $\sim 5''$ of SNB04.

The southern molecular core containing the G34.4 UC HII region contains three overlapping flows seen in the CO emission (flows 'C', 'D' and 'E'). Blue-shifted CO, ^{13}CO and $C^{18}O$ gas is seen toward the G34.4 UC HII region extending to the West (flow G34.4:C). This

outflow is seen most clearly in ^{13}CO and C^{18}O emission in Figure 4. ^{13}CO blue-shifted emission is traced back to the HII region (top right panel in Fig. 4) while the bottom two panels illustrating the velocity structure in the dense gas show that blue-shifted emission extends from the UC HII region to the west. A possible red-shifted outflow lobe east of the UC HII may be visible in ^{13}CO emission in the top right panel in Fig. 4 although the identification is not definitive.

The NE-SW flow (G34.4:D) appears to be centered about 10″ SE of the UC HII region, just off the peak of a dense C^{18}O clump. The flow appears to be relatively symmetric in the red and blue-shifted gas distribution although the actual morphology is considerably confused due to overlapping outflows. If the flow is symmetric, then one would expect the driving source to be located near the small, filled triangle at $18^{\rm h}53^{\rm m}19.0^{\rm s}$, 01°24′35″ along the G34.4:D outflow axis in Figs. 3 & 4.

The SE-NW flow (G34.4:E) is seen clearly in both CO and ^{13}CO emission. If the driving source is located between the red- and blue-shifted emission along the outflow axis, it would be centered about 5″ S-SW of the UC HII region (indicated by a small, filled triangle at $18^{\rm h}53^{\rm m}18.6^{\rm s}$, 01°24′43″ along the G34.4:E outflow axis in Figs. 3 & 4). The outflow is not symmetric: the red-shifted emission lobe extends about 20″ to the SE while the blue-shifted lobe extends roughly 60″ to the NW, overlapping the blue-shifted lobe from the G34.4 UC HII region flow and the red-shifted lobe of flow G34.4:A farther north.

Outflow G34.4:A has a position angle of +58° (measured from North to the axis of the blue-shifted lobe) while G34.4:B P.A. = –38° and the difference in orientation between outflow axes is 96°. The positions angles of the three outflows near the G34.4 UC HII region are: G34.4:C P.A. = –100°; G34.4:D P.A. = +38°; G34.4:E P.A. = –34° and the maximum difference in orientation between the axes is 138°.

3.2. Mass & Kinematics of the Outflows

The mass associated with CO line emission is calculated following Scoville et al. (1986). The CO excitation temperature is taken to be 34 K which is the dust temperature in MM1 derived from fits to the SED (Rathborne et al. 2005). We assume the gas is in LTE with $[{\rm CO}]/[{\rm H_2}] = 10^{-4}$, $[{\rm CO}]/[^{13}{\rm CO}] = 51$ and $[{\rm CO}]/[{\rm C}^{18}{\rm O}] = 378$ at the galacto-centric distance of 5.8 kpc (Wilson & Rood 1994).

The CO optical depth at red and blue-shifted velocities is estimated from the CO/^{13}CO ratio of spectra taken at four positions in the mosaic image that have been convolved with a 10″ beam. The open triangles in the top, center panel of Fig. 4 show the locations where the

spectra were taken, while Figure 8 shows the spectra taken at those positions. In channels where no ^{13}CO is detected, we assume that the CO is optically thin. The CO and ^{13}CO line profiles show a dip near $v_{\rm LSR}$ indicating that the lines suffer from self-absorption and/or the interferometer is missing extended flux at lower velocities.

Because multiple, overlapping flows are present, it is not possible to obtain a reasonable estimate of the inclination of each flow. Thus, we assume an inclination angle of 45° which minimizes errors introduced by inclination effects for flows that are not near the plane of the sky or along the line-of-sight. Table 1 summarizes the physical properties of the molecular gas in the combined outflows originating from G34.4 MM and those centered near the UC HII region. The total flow mass M_f is given by $\sum M_i$ where M_i is the flow mass in velocity channel i corrected for optical depth. The momentum P is given by $\sum M_i v_i$ and the kinetic energy E by $\frac{1}{2}\sum M_i v_i^2$ where v_i is the central velocity of the channel relative to v_{LSR}.

The dynamical timescale t_d is calculated using $R_f / < V >$, where the intensity-weighted velocity $< V >$ is given by $P/(\sum M_i)$ (Cabrit & Bertout 1990) and R_f is the average outflow radius of the flows. This method of calculating t_d is really only correct for a single outflow; however, an independent outflow age cannot be determined for both flows in the cores since they cannot be separated near the central position. Because of this uncertainty, the flow dynamical timescale could easily be in error by a factor of 2 to 5.

The mass outflow rate $\dot{M}_f$ is $\sum M_i/t_d$, the force F is P/t_d and the mechanical luminosity L is E/t_d. Since these values are dependent on t_d^{-1} uncertainties in t_d are directly applicable to $\dot{M}_f$, F, and L.

The combined outflows from the G34.4 core have a total mass of 111 $M_\odot$ and energy, E $= 7.8\times10^{46}$ ergs. The G34.4 MM outflows have a combined mass 34.8 $M_\odot$, E $= 4.9\times10^{46}$ ergs. Despite the uncertainties, the flow masses and energies are consistent with those for outflows driven by young, early B stars.

3.3. The dense gas cores

The C^{18}O and ^{13}CO moment 0 images (Fig. 4) show clearly that the two cores have very different characteristics. The southern core centered on the G34.4 UC HII region is extended, with a largest spatial scale of about 1.4 pc at a distance of 3.9 kpc. The northern core, centered on G34.4 MM, is significantly more compact with higher peak emission than the southern cloud. The diameter of the G34.4 MM core is about 0.2 pc and is surrounded by faint, diffuse ^{13}CO emission that extends out to about 1 pc in size.

The total mass of the 2 cores as measured from $C^{18}O$ is given in Table 2. $C^{18}O$ is assumed to be optically thin although this is not likely to be true near v_{LSR} at the peak of the line profile. The extended, southern cloud in which the UC HII region is embedded is almost 10 times more massive ($692\,M_\odot$) than the G34.4 MM core ($75\,M_\odot$).

As Fig. 8 illustrates, the $C^{18}O$ line appears to be suffering from missing flux due to the lack of short baselines. This is most apparent in the spectra taken SE of the UC HII region position where $C^{18}O$ is more extended and there is a clear double peaked line profile. The $C^{18}O$ line is single peaked closer to the cloud core suggesting that the interferometer is recovering most of the flux density and we are not seeing significant self-absorption. Thus, the mass estimates based on $C^{18}O$ are lower limits.

The G34.4 and G34.4 MM molecular cores have a projected separation of about 40″ (0.75 pc at 3.9 kpc). Their LSR velocities as measured by the peak of the $C^{18}O$ line differs by $1.4\,km\,s^{-1}$.

3.4. Mid-Infrared Sources: GLIMPSE & MIPSGAL

G34.4 MM and the G34.4 UC HII region are embedded in an extended, filamentary IR-dark cloud complex seen against the diffuse PAH background emission which is visible primarily in the Spitzer 8.0 μm band (Figures 1 & 2). The G34.4 MM core is associated with diffuse emission in all 4 IRAC bands, but is particularly noticeable at 4.5 μm. The [4.5] band contains the H I Brα line along with some molecular forbidden lines, notably the CO 1-0 P(8) fundamental band-head, but, unlike the other 3 bands, does not contain any PAH emission feature. The [4.5] band also contains several H_2 lines (e.g. the H_2 0-0 S(9) line at 4.694 μm) which trace shocks in some massive outflows (e.g. DR21: Smith et al. 2006; W75N: Davis et al. 2006). Thus, the [4.5] band appears to readily trace ionized and/or shocked gas.

Figure 9 shows the IRAC 4.5 μm image in greyscale with ^{13}CO contours overlayed for reference. The plus symbols represent the locations of the UC HII region and G34.4 MM core. The open diamonds just south and south-east of the UC HII region represent the predicted locations of sources driving outflows G34.4:E ($18^h53^m18.6^s$, 01°24′43″) and G34.4:D ($18^h53^m19.0^s$, 01°24′35″) based on CO and ^{13}CO emission. While the predicted position of the YSO that was identified based on the CO outflow morphology should be considered no better than an educated guess, it is interesting that each position is associated with a mid-IR source to within a few arcsec. The characteristics of these sources along with other sources in the cluster are discussed below.

The spectral energy distributions (SEDs) were analyzed by fitting model SEDs to each observed source from a large pre-computed grid of YSO models (Robitaille et al. 2006, 2007). The grid consists of 20,000 2-D YSO radiation transfer models spanning a complete range of stellar mass and evolutionary stage. Each YSO model outputs SEDs at ten viewing angles (inclinations), so the fitter actually has 200,000 SEDs to choose from. The YSO models also output SEDs for each of 50 aperture sizes. Thus, if the distance to the star formation region is known, only the model SEDs with the appropriate aperture size compared to the observed photometry are used. A grid of stellar atmospheres were also incorporated into the fitting algorithm in order to facilitate the separation of main-sequence and evolved stars from YSOs (Brott & Hauschildt 2005; Kurucz 1993). The fitting algorithm includes a foreground extinction component to the model which allows one to easily distinguish highly reddened stars from YSOs which have an additional emission component in the mid-infrared.

The 24 μm fluxes were cross correlated with positions of the 2199 GLIMPSE Archive sources lying within a 3.9′ radius of the G34.4 UC HII region to account for observational errors in addition to photon counting statistics. For the purposes of the fitting, all flux uncertainties that fell below the 10% level were reset to a minimum value of 10%. The SED fitter was then run on this combined 8-band source list, fitting only the fluxes of sources detected in 4 or more bands. Sources with SEDs well fit by a stellar atmosphere are not likely to be cluster members. Sources with a χ^2 per flux data point ($\chi^2/N_{\rm data}$) of 4.8 provided a reasonable dividing line between sources that, by eye, appeared to be well-fit by stellar atmospheres and those that were not well-fit due to IR excesses. Of the total 2199 sources in the GLIMPSE Archive in this region, 868 were detected in four or more bands. Of those, 829 sources were well-fit by stellar atmospheres and thus are likely foreground or background stars rather than YSO cluster members. The remaining sources were fit with YSO models and 27 of these met the $\chi^2/N_{\rm data} \leq 4.8$ criterion. Of the 9 sources that were not well-fit either by stellar atmospheres or YSO SEDs, 1 appears to be a YSO and 8 are probably Archive sources with improperly extracted fluxes in one or more bands or there was a mismatch of GLIMPSE with 2MASS or MIPS sources.

An overview of the results of the SED fitting procedure is presented in Figure 10 and Tables 3 & 4. Most of the filamentary dark cloud is visible in the three-color image (Fig. 10) in which red corresponds to MIPS 24 μm, green to GLIMPSE 8 μm and blue to GLIMPSE 4.5 μm. The G34.4 complex is located near the center of Fig. 10 (in the region outlined with a large, white circle). Point sources are marked by small circles color-coded by source type as identified by the Fit flag in Table 3. Sources that were well-fit as YSOs are marked by green circles and given a Fit flag of 1 in Table 3. The yellow circle identifies a probable YSO that was not well-fit (Fit = 2). Blue circles identify sources that were well-fit by stellar photospheres. MIPS 24 μm point sources that are detected in fewer than 3 of the

2MASS+IRAC bands and hence were not run through the fitter (Fit=4) are identified by red circles; the majority of these are probably YSOs. The cyan circle (source 32 located between sources 8 and 10 in Fig. 10) marks the Archive source that coincides with the proposed origin of outflow G34.4:D, it is detected only at 3.6 and 4.5 μm, and hence was not run through the fitter (Fit=3). The area covered by the OVRO observations is contained primarily within the large white circle, which is referred to as "region C" in Table 3. "Region N" is identified by the box north of region C, while "region S" is identified by the box to the south. The G34.4 UC HII region appears white in this image because it is bright in diffuse emission at all wavelengths. There are two prominent MIPS sources: G34.4 MM and another, fainter source located about 2′ north of G34.4 MM at position $18^{\rm h}53^{\rm m}20.602^{\rm s}$, $+01°28'25.61''$.

Table 3 presents a summary of the positions and fluxes in each band for all identified probable YSO cluster members in and near the dark cloud. Table 4 presents the best fit model parameters for each YSO with enough flux points to be fitted. Output model parameters are: interstellar extinction to the source, A_V; stellar mass, $M_\star$; total luminosity of the YSO, $L_\star$; envelope accretion rate, $\dot{M}_{\rm env}$; and inclination, i. Note that A_V does not include the extinction produced by a circumstellar disk or envelope and thus it represents a lower limit for YSOs with significant circumstellar material. In general, each source can be well fit by multiple YSO SED models and this generates a corresponding range of the best-fit model parameters. For well-fit YSOs, results of all fits with $\Delta\chi^2/N_{\rm data} \leq 1$ relative to the best-fit model are reported. E.g., for a typical source detected in $N_{\rm data} = 5$ bands, all fits with $\Delta\chi^2 \geq 5$ with a formal probability relative to the best fit of less than $\exp(-\Delta\chi^2/2) = 0.08$ are excluded. The cumulative probability distribution for each parameter is then constructed using the Gaussian-weighted probability of each fit relative to the best fit. A range of parameter values that has a greater than 95% probability of containing the actual value for the source is then determined and reported in Table 4.

The central region of the filament:
In the region for which CO outflow data is determined, 7 YSOs with good fits have been identified (sources 6-12), along with one poorly-fit, possibly massive YSO (source 31 in tables 3 & 4) located on the northeast edge of the G34.4 MM 24 μm emission. Source 12, the highly luminous, the mid-IR counterpart to G34.4 MM, is most likely the driving source of outflow G34.4:A. Marked by a larger green circle in Figure 10, source 12 is partially resolved in the GLIMPSE images (this is seen most clearly in the 4.5 μm greyscale image in Fig. 9). The morphology of source 12/G34.4 MM is consistent with two dust emission lobes separated by an absorption lane due to a disk where the lobes are in rough alignment with the axis of outflow G34.4:A.

The fluxes in the two lobes of source 12/G34.4 MM in each GLIMPSE band was summed

and combined with the point-source fluxes from *MSX* 21.3 μm (Price et al. 2001), MIPS 24 μm and MIPS 70μm to model the source SED across the mid-IR. The 10 best fits to source 12/G34.4 MM are plotted in Figure 11. The fit parameters are well-constrained and the best fit has $\chi^2 = 6.62$ which is significantly lower than the second-best fit with $\chi^2 = 20.79$. The best fit parameters suggest a massive YSO with $M_\star \sim$14 $M_\odot$, $L_\star \sim$ 9,400 $L_\odot$. The source is deeply embedded, behind greater than $A_V \sim 40$ mag of extinction and it is young with a high envelope accretion rate of $\dot{M}_{\rm env} \sim 10^{-3}$ $M_\odot$ yr^{-1}.

The inclination angle of the best-fit model is $i = 56°$, consistent with the orientation of outflow G34.4:A which has a wide opening angle of 43° but does not intersect the plane of the sky. This interpretation assumes that a single YSO dominates the flux density and geometry of the mid-IR emission. Given that two outflows have been identified emanating from the G34.4 MM core and the far-IR fluxes exceed those predicted by a single YSO SED, more than one YSO is likely present. However, the resolution of the GLIMPSE images is not adequate to clearly distinguish between sources that are likely to drive outflows G34.4:A and G34.4:B.

For the remaining six well-fit YSOs in region C, the best fit models are presented in Figure 12a while the distribution of their corresponding best-fit masses and luminosities are shown in Figure 12b. Of these, two YSOs (sources 10 & 11) are nearly coincident with the UC HII region.

Source 11 is a luminous YSO located near the projected center of the UC HII region and appears to be the most likely candidate to drive outflow G34.4:C. The GLIMPSE position differs from the 6 cm ionized gas peak by $\sim 1.3''$. This could be due to differences in astrometry between the radio and IR data; however, the discrepancy exceeds the GLIMPSE astrometric uncertainty of $0.3''$ and the Very Large Array estimated uncertainty of $\sim 0.1''$. It is more likely that the centimeter peak tracing the ionized gas is offset from the actual YSO. This could easily happen if the ionized gas morphology closely follows the confines of a bipolar outflow cavity. It is also possible that the center of the source is not detected in the IRAC bands due to high extinction or the bright diffuse background of the UC HII region itself. We may only see the warm outflow cavity associated with the blue-shifted lobe in the mid-IR that is displaced from the centimeter continuum emission.

Both sources 10 and 11 suffer from confusion with the UC HII region at IR wavelengths longward of the IRAC bands. The UC HII region emits very strongly in all 4 *MSX* bands and in MIPS 24 and 70 μm. These fluxes were used as upper limits for the fits to sources 10 and 11, but they are very high limits (see Figure 12a), and the fits to both sources are poorly constrained. The best fit results for source 11 suggest $M_\star$ =2–10 $M_\odot$ and $L_\star$ =200–5,200 $L_\odot$, but the probability distribution of fit parameters shown in Figure 12b is skewed

and allows for higher masses and luminosities up to $M_\star \sim 20$ M$_\odot$, $L_\star \sim 45,000$ L$_\odot$ (albeit at a formal probability level of only a few percent). SNB04 determined a spectral type of B0.5 ($L_\star \sim 40,000$ L$_\odot$) for the central star of the G34.4 UC HII region assuming a single zero-age main sequence (ZAMS) star is producing the observed Lyman continuum flux. Thus, if source 10 is the ionizing star of the UC HII region, the higher values of mass and luminosity are more plausible.

Due to its physical location between the red and blue-shifted lobes of outflow G34.4:E, source 10 appears to be the most probable driver of this outflow. The best fit results suggest that it is a YSO with M$_\star$ =0.5–10 M$_\odot$ and L$_\star$ =45–4,500 L$_\odot$. Again, the association of this YSO with strong outflow activity suggests that the upper end of this range of mass and luminosity may be more appropriate.

Source 32 (cyan circle), the potential driver of outflow G34.4:D, is detected in only two IRAC bands ([3.6] and [4.5]) at the 5σ level sufficient for inclusion into the GLIMPSE Archive. Based on these two bands, source 32 has a red color of $[3.6] - [4.5] = 1.3$ which is consistent with it being a YSO (Robitaille et al. 2006). The lack of GLIMPSE Archive fluxes in bands [5.8] and [8.0] means that this source was not detected at the 3σ level in those two bands, corresponding to magnitudes fainter than 13.0 in each band[2]. The colors of YSO models for very young sources predict $[3.6] - [5.8] > 0.4$ and $[5.8] - [8.0] > 0.4$, corresponding to magnitudes fainter than 13.6 and 13.2 in bands [5.8] and [8.0], respectively (Robitaille et al. 2006). Thus the non-detection in bands [5.8] and [8.0] is consistent with the interpretation that source 32 is a YSO.

Source 32 is also not detected in the MIPS 24 μm band. However, given the proximity to the very bright UC HII and lower resolution of MIPS compared to IRAC, this source is confused with the PSF wings of the UC HII region. Based on an estimate of the MIPS sensitivity in a confused region, a 3σ upper limit of 50 mJy (magnitude 5.4) is expected for the 24 μm flux. This could potentially allow a very red $[3.6] - [24] \approx 8.6$ color for this source. We therefore conclude that the mid-IR colors of source 32 are consistent with those for a YSO, however the strongest evidence for this remains the fact that it lies along the CO outflow axis of G34.4:D near where one might expect the driving source to be located.

In summary, 9 YSOs have been identified and characterized in region C near G34.4 MM and the UC HII region. Four or five are probably massive with $M_\star > 8$ M$_\odot$ while the others are low-to-intermediate mass with $M_\star$ between 0.5 and 8 M$_\odot$.

---

[2]See the GLIMPSE Quality Assurance Document at http://www.astro.wisc.edu/glimpse/GQA-master.pdf

The northern filament:
North of the G34.4 MM and UC HII region complex (in region N) 17 YSOs have been successfully identified based on fits to the SEDs. Most of these YSOs closely trace the IR-dark cloud structure. At the extreme north end of the field there is another 24 μm bright source (source 29 in Tables 3 & 4) that may be similar to but less massive than G34.4 MM. The SED is well-fit with $\chi^2 = 17.39$ suggesting a YSO with $M_\star$ ~4.8–6.8 $M_\odot$ and $L_\star$ ~170–340 $L_\odot$. The remaining 16 YSOs in region N are less massive than Source 29 with mass estimates between about 0.5 and 6.5 $M_\odot$.

The southern filament:
The southern part of the IR-dark filament (region S) contains 5 sources with SEDs that are well-fit as YSOs. Five relatively faint 24 μm sources that are likely to be YSOs are also scattered throughout this region. Sources in this southern region are more distributed and are not spatially well-correlated with the dark cloud filament. This is in contrast to the YSOs in the northern region where they follow the cloud boundaries reasonably well. Mass estimates range from about 1 to 7 $M_\odot$.

4. Discussion

The IR-dark cloud associated with IRAS 18507+0121 has a filamentary structure that spans more than 9′ on the sky (> 10 pc at 3.9 kpc). Splitting the cloud into three regions (south, central and north) one finds that the southern region is associated with mostly low to intermediate-mass YSO candidates (10 in total) that are not spatially well-correlated with the dark cloud filament. The northern segment of the filament contains 23 low to intermediate-mass YSO candidates that tend to trace the IR-dark cloud structure. The central region of the filament is in the process of forming four or five mid- to early-B stars with $M_\star > 8\,M_\odot$. Four more sources are likely low-to-intermediate mass with $M_\star$ between 0.5 and 8 $M_\odot$. Together with an additional 11 YSO candidates seen at 24 μm this central region harbors a relatively compact cluster with a total of 20 YSO candidates.

4.1. GLIMPSE-detected source characteristics

Bright emission in the 4.5 μm Spitzer IRAC can be a strong indicator of molecular outflow (e.g. Qiu et al. 2007, Smith et al. 2006, Noriega-Crespo et al. 2004). The most likely reason for this is the presence of H_2 emission lines and/or emission from the CO 1-0 P(8) bandhead. All four IRAC bands contain H_2 emission lines, but these features are

narrow and hence can only significantly enhance the brightness in the broadband images if the lines are extremely bright relative to the continuum. Because H_2 features are distributed throughout the IRAC bands, strong H_2 lines will not cause a greater enhancement of the flux in band [4.5] than in bands [5.8] and [8.0] (see e.g., Smith et al. 2006). In contrast, the CO 1-0 P(8) emission bandhead is a broad feature that occupies the entire [4.5] filter and can become bright in the presence of shocked, molecular gas. There is not significant CO bandhead emission in the remaining IRAC bands. Thus, sources with *excess* emission in band [4.5] relative to bands [5.8] and [8.0] appear likely to have CO bandhead emission resulting from shocked, molecular gas. This does not preclude the possibility that significant H_2 emission may also contribute to the brightness in all IRAC bands.

Three of the 29 YSOs listed in Table 3 that were detected in all four IRAC bands have noticeable excess emission at 4.5μm and strong flux at 24μm: sources 6 & 12 in region C, and source 29 in region N. Because of this, SED fits used the [4.5] fluxes as upper limits only since the YSO SED models do not incorporate molecular line emission. These sources are likely to have significant shocked, molecular gas and are undergoing outflow & accretion. Source 31, although it was not well-fit, should probably be considered in this group as well. It was not well-fit because it has a strong 4.5μm excess and it was only detected in the four IRAC bands. The SED (not shown) looks similar to G34.4 MM itself. Further, its non-detection at 24μm is almost certainly due to its proximity to G34.4 MM.

The most prominent of the 4.5μm excess sources is source 12, the mid-IR counterpart to G34.4 MM and outflow G34.4:A. The association of this source with the CO outflow favors the interpretation that the 4.5μm excess is due to shocked CO emission.

The potential drivers of outflows G34.4:C (source 11) and G34.4:E (source 10) do not show similar 4.5μm excess fluxes. A possible reason for this may be that they are somewhat more evolved than source 12. In very young sources, particularly those with $M_\star > 2$ $M_\odot$, high accretion rates create a cool, distended photosphere that does not emit strongly enough in the UV to excite the PAH emission features present in the IRAC [3.6], [5.8] and [8.0] bands. In more evolved sources, however, PAH emission can hide the contrast between [4.5] and the other 3 bands. Alternatively, as discussed above, both sources 10 and 11 suffer from confusion with the UC HII region which emits strongly in all four bands and this could also mask moderate enhancements due to CO bandhead emission.

As a final note, three sources show marginal excess at 4.5μm relative to bands [5.8] and [8.0]: source 7 in region C and sources 20 & 26 in region N. These sources do not appear to have strong emission at 24μm, so they may be a different type of source than those with strong 4.5 & 24μm excesses.

4.2. Timescale for Massive Star Formation

There are two cloud cores in the central region of the filament: one more massive core in the south surrounded by a more diffuse molecular cloud that contains the UC HII region and one that is more compact containing source 12/G34.4 MM. The cores are separated by about 0.75 pc. Each cloud core is producing a small cluster of massive flows that look similar and are of similar ages although the northern outflows associated with G34.4 MM have about one third the mass as the southern flows.

Due to the shorter formation timescales ($\lesssim 10^5$ years), massive (proto)stars begin to burn hydrogen even while they continue to accrete material. The generation of a UC HII region identifies which sources have reached the main sequence and begun hydrogen burning while the detection of a molecular outflow traced to the source identifies whether it is still accreting (and hence still powering an outflow). However, the addition of material onto the stellar surface implies that the source will move up the main sequence. In this sense it is still a *protostar* because it has not reached its final mass.

The central source in the G34.4 UC HII region (source 11) has a spectral type of B0.5 while the spectral type of source 12/G34.4 MM is probably closer to a B2 star (this work & SNB04). High-velocity CO emission can be traced to both sources suggesting that they are still accreting even though they have reached the main-sequence.

The characteristic time scale of the outflow/infall phase from early B stars is roughly a few $\times 10^5$ years (Richer et al. 2000) while the evolutionary timescale for a B0.5 star to reach the main-sequence is roughly 10^5 years. Since ionized gas is seen toward both cores and the outflow characteristics are similar, it seems reasonable to assume that they began forming massive stars at approximately the same time: about 10^5 years ago.

SNB04 detected a lower mass population of this cluster (e.g. a few solar masses or less) at near-infrared wavelengths (see their Fig. 6). Their detected cluster population was more distributed, less embedded and less massive than those detected in this work. They found that this sub-population is less than 3 Myrs old but probably more than 0.3 Myrs old.

There are numerous problems associated with these age estimates and they could be in error easily by a factor of a few. However, let us take them at face value for now. SNB04 discovered a distributed population of low to intermediate mass stars that may have formed a few Myrs ago. The more massive stars detected in this work are more tightly associated with the dense molecular gas (as expected) and appear to be somewhat younger, more like 10^5 years old. This suggests that the star formation in this cold, dark cloud may have formed in two stages: first lower mass stars began to form, then, a few Myrs later, the more massive, early B stars began to form.

Such a situation is predicted when clouds have magnetic fields that are stronger than needed to provide support against gravitational collapse and the core mass to magnetic flux ratio (M/Φ) is sub-critical. Thus, low-mass stars would form in originally highly magnetically sub-critical clouds, with ambipolar diffusion leading to core formation, quasi-static contraction of the cores, and eventually, massive star formation (see e.g. the review by Ward-Thompson et al (2007) and references therein). If this scenario is correct, then the cold, dark filament associated with IRAS 18507 may provide an example of a cloud with delayed massive star formation due to an initially high magnetic field and sub-critical M/Φ.

4.3. Star Formation Efficiency

The set of best-fit SED models for YSO candidates can be used to construct a χ^2-weighted probability distribution of the best-fit model parameters. We sum the mass probability distributions for each source to construct mass functions for all well-fit YSOs (Fit=1) in Tables 3 & 4. The total mass of the GLIMPSE-detected YSOs in this IR-dark cloud is then $127 \pm 27\,\mathrm{M}_\odot$.

The total stellar mass of the central (sub)cluster containing G34.4 MM and the UC HII region is $48 \pm 20\,\mathrm{M}_\odot$(or $\sim 38\%$ of the total detected stellar mass). About $14\,\mathrm{M}_\odot$ is in source 12/G34.4 MM, $10\,\mathrm{M}_\odot$ is in source 31 (the yellow source near G34.4 MM in Fig. 10), and the remaining $24\,\mathrm{M}_\odot$ of stellar mass resides in the central star producing the UC HII region and its surrounding cluster. These rough stellar mass estimates are incomplete for $M_\star < 3\,\mathrm{M}_\odot$. They also do not include the additional 20 YSO candidates that were detected at 24 μm but in fewer than three IRAC bands. Thus, the stellar mass estimate should be considered a lower limit.

Using the initial mass function (IMF) of Kroupa et al. (2001) (where the IMF slope follows a Salpeter IMF for $M_\star > 1\,\mathrm{M}_\odot$ and it becomes shallower for $0.1 < M_\star < 1\,\mathrm{M}_\odot$) one can estimate the expected stellar mass for $M_\star < 3\,\mathrm{M}_\odot$. Assuming $127 \pm 27\,\mathrm{M}_\odot$ of mass in stars more massive than $3\,\mathrm{M}_\odot$, roughly $413 \pm 103\,\mathrm{M}_\odot$ of mass is expected to be in the form of stars less massive than $3\,\mathrm{M}_\odot$. Thus, the total stellar mass content of this cloud is expected to be $\sim 540 \pm 130\,\mathrm{M}_\odot$.

This stellar mass estimate is a little more than half of the derived mass of the ammonia hot core of $1000\,\mathrm{M}_\odot$ surrounding the UC HII region (Maralles, Rodrígues & Scalise 1994). And it is about 7% of the cloud mass of $7500\,\mathrm{M}_\odot$ derived from 1.2 mm continuum emission (Rathborne et al. 2005). The total star formation efficiency is then $M_\star/(M_{cloud} + M_\star) = 540/(8040) \sim 0.07$ or 7%. This should be considered an upper limit

because 1.2 mm continuum emission traces warm dust (typically 30-50 K) which is heated predominantly by massive stars - it does not effectively trace the cold gas and dust (5-10 K) which may represent the bulk of the total cloud mass.

We can also obtain an estimate of the massive and intermediate mass star formation efficiency in the warm gas traced by 1.2 mm continuum emission and in the densest part of the hot core. Assuming a warm cloud mass of 7500 $M_\odot$ and a total mass of stars with $M_\star > 3\,M_\odot = 127\ M_\odot$, the massive star formation efficiency is roughly 2%.

4.4. Can the outflows destabilize the cloud cores?

The G34.4 cloud core surrounding the UC HII region:
Maralles, Rodrígues & Scalise (1994) estimated a mass of the G34.4 cloud core surrounding the UC HII region to be $\sim 1000\,M_\odot$ based on NH_3 observations. They only detect emission near the UC HII region, not near the G34.4 MM core. The $C^{18}O$ mass estimate of $693\,M_\odot$ compares reasonably well with that of NH_3 given the uncertainties inherent with both estimates and the fact that our $C^{18}O$ map is missing extended emission.

If we take the mass of the G34.4 core surrounding the UC HII region to be $M_{cloud} = 1000\,M_\odot$ we find that the core has about nine times more mass than in the high-velocity molecular outflows. The gravitational binding energy of the cloud, can be calculated from $GM_{cloud}^2/c_1 r$, where c_1 is a constant which depends on the mass distribution ($c_1 = 1$ for $\rho \propto r^{-2}$). We find that the gravitational binding energy is 2.4×10^{47} ergs. Roughly 11% of the molecular cloud core is participating in the outflow and the combined outflow energy is roughly one third the gravitational binding energy of the cloud. The G34.4 outflows near the UC HII region are injecting a significant amount of mechanical energy into the cloud core and may help prevent further collapse of the cloud. However, they are not likely to totally disrupt the cloud. As long as cloud material remains, this leaves the door open for possible future episodes of star formation.

The compact G34.4 MM cloud core:
SNB04 estimate the mass of the G34.4 MM core based on 2.6 millimeter thermal dust emission to be between 150 and 650 $M_\odot$ with 240 $M_\odot$ being the value derived for an opacity index, β of 1.5 and a temperature of 50 K. Our estimated mass based on $C^{18}O$ emission is significantly less than this ($\sim 75\,M_\odot$) suggesting that our $C^{18}O$ maps are missing extended emission or the assumptions used to estimate the mass associated with warm dust emission in the G34.4 MM core were not correct. Thus, for example, if $\beta = 0.7$ and $T_d = 70$ K then the mass of the millimeter core would be $\sim 75\,M_\odot$ which is consistent with the mass derived from

$C^{18}O$. Such a low opacity index and high temperature could be caused by the presence of strong shocks through most of the core mass which would prevent large grains from forming and maintain the bulk of the gas at higher temperatures. Indeed, this could be possible given the small size of the core (0.2 pc) and the fact that two outflows with a combined mass of nearly 35 $M_\odot$ are blasting their way out of the core.

If we assume a mass of 75-240 $M_\odot$ for the G34.4 MM core, as derived from the $C^{18}O$ and 2.6 mm continuum observations, then the gravitational binding energy of the cloud is 5.6×10^{45} ergs to 5.7×10^{46} ergs. The kinetic energy of the outflowing gas is between 1.2 to nearly nine times the gravitational binding energy of the cloud core. Thus, the G34.4 MM flows appear to have more energy relative to the core and are more likely to disrupt the compact core. Therefore we may be seeing the first and only episode of massive star formation in this compact region.

5. Summary

We have observed the central region of the IR-dark cloud associated with IRAS 18507+0121 in CO J=1–0, ^{13}CO(J=1−0) and $C^{18}O$(J=1−0) with the Owens Valley Radio Observatory at $\sim 4''$ resolution. Five massive outflows from two cloud cores were discovered. A total of 146 $M_\odot$ of material is participating in the combined outflows and injecting $\sim 1.3 \times 10^{45}$ ergs of kinetic energy. We also used archived Spitzer data from the GLIMPSE survey to gain an understanding of the stellar content of the cluster and the entire IR-dark filament. Modeling of the SEDs of GLIMPSE sources identified 31 young stellar objects in the filament with a combined stellar mass of $\sim 127 \pm 27\, M_\odot$. An additional 22 sources were identified as probable cluster members based on the presence of strong 24 μm emission.

The total star formation efficiency in the G34.4 cloud filament is estimated to be about 7% while the massive and intermediate mass star formation efficiency in the entire cloud filament is estimated to be roughly 2%.

A qualitative evaluation of the outflow characteristics and presence of ionized gas in the central region of the IR-dark cloud filament suggests that the early B stars currently undergoing outflow and accretion began forming stars at approximately the same time: about 10^5 years ago. A population of lower mass stars were detected by SNB04 that appear to have an age of about a few Myrs. This dual population suggests that stars in the IRAS 18507 cloud may have formed in two stages: first lower mass stars formed and then, a few Myrs later, the more massive, early B stars began to form. Such a situation can occur in magnetically sub-critical clouds in which slow, ambipolar diffusion leads to the delayed onset

of core contraction and eventual massive star formation.

A comparison of the gravitational binding energy with the outflow kinetic energy in the two cloud cores studied in molecular lines suggests that the compact core containing G34.4 MM is being destroyed by its molecular outflows. The outflows have as much or more kinetic energy than the gravitational binding energy of the cloud core. Thus, we may be seeing the first and only episode of massive star formation in this compact region.

In contrast, the 690 $M_\odot$ core surrounding the G34.4 UC HII region has twice the gravitational binding energy as the combined outflow kinetic energy. Thus, although the outflows are injecting a significant amount of mechanical energy into the cloud core and may help prevent further collapse of the cloud, they are not likely to totally disrupt the cloud. As long as cloud material remains, this leaves the door open for possible future episodes of star formation.

Acknowledgments
DSS would like to thank Allison Sills for useful discussions on properties of young clusters. Research at the Owens Valley Radio Observatory is supported by the National Science Foundation through NSF grant number AST 96-13717. Star formation research at Owens Valley is also supported by NASA's Origins of Solar Systems program, Grant NAGW-4030, and by the Norris Planetary Origins Project. LB acknowledges support from the Chilean Center for Astrophysics FONDAP grant 15010003. Support for GLIMPSE, part of the Spitzer Space Telescope Legacy Science Program, was provided by NASA through contracts 1224653 (University of Wisconsin at Madison) and 1224988 (Space Science Institute). BW gratefully acknowledges support from the NASA Astrophysics Theory Program (NNG05GH35G) and the Spitzer Space Telescope Theoretical Research Program (Subcontract 1290701).

REFERENCES

Blake, G.A., Sutton, E.C., Masson, C.R., Phillips, T.G 1987, ApJ, 315, 621

Bohlin, R. C., Savage, B. D., & Drake, J. F. 1978, ApJ, 224, 132

Bronfman, L., Nyman, L., & May, J. 1996, A&AS 115, 81

Brott, I., & Hauschildt, P. H. 2005, in ESA SP-576: The Three- Dimensional Universe with Gaia, ed. C. Turon, K. S. O'Flaherty, & M. A. C. Perryman, p. 565

Carey, S. J., Noriega-Crespo, A., Price, S. D., et al. 2005, BAAS, 207, 6333

Carral, P. & Welch, W. J. 1992, ApJ, 385, 244

Churchwell, 1999, in "The Origin of Stars and Planetary Systems", ed. Charles J. Lada and Nikolaos D. Kylafis (Kluwer Academic Publishers), p. 515

Davis, C. J., Kumar, M. S. N., Sandell, G., Froebrich, D., Smith, M. D., & Currie, M. J. 2006, MNRAS, 374, 29

Edris, K. A., Fuller, G. A. & Cohen, R. J. 2007, A&A, 465, 865

Faúndez, S., Bronfman, L., Garay, G., Chini, R., Nyman, L.-A & May, J. 2004, A&A, 426, 97

Fazio, G. G. et al. 2004, ApJS, 154, 10

Qiu, K., Zhang, Q., Gutermuth, R. A., Megath, S. T., Beuther, H., Sridharan, T. K., Shepherd, D. S., Testi, L., & De Pree, C. G. 2007, BAAS, poster presented at the January 2007 AAS meeting.

Hildebrand, R. H. 1983, Q.Jl.R.astr.Soc, 24, 267.

Kramer, C., Alves, J., Lada, C., Lada, E., Sievers, A., Ungerechts, H., & Walmsley, M. 1998, A&A, 329, L33

Kroupa, P. 2001, MNRAS, 322, 231

Kurucz, R. 1993, ATLAS9 Stellar Atmosphere Programs and 2 km/s grid. Kurucz CD-ROM No. 13. Cambridge, Mass.: Smithsonian Astrophysical Observatory, 1993, 13

Meyer, M. R., & Beckwith, S. V. W. 2000, in "ISO Survey of a Dusty Universe," eds. D. Lemke, M. Stickel, & K. Wilke, Lecture Notes in Physics, vol. 548, p. 341

Miralles M. P., Rodriguez, L. F., & Scalise, E. 1994, ApJS, 92, 173

Molinari S., Brand, J., Cesaroni, R., & Palla, F. 1996, A&A, 308, 573

Molinari, S., Brand, J., Cesaroni, R., Palla, F., & Palumbo, G. G. C. 1998, A&A, 336, 339

Noriega-Crespo, A., Morris, P., Marleau, F. R., Carey, S., Boogert, A., van Dishoeck, E., Evans, N. J. II, Keene, J., Muzerolle, J., Stapelfeldt, K., Pontoppidan, K., Lowrance, P., Allen, L. & Bourke, T. L. 2004, ApJS, 154, 352

Palla, F., & Stahler, S. W. 1993, ApJ, 418, 414

Palla, F., Brand, J., Comoretto, G., Felli, M., & Cesaroni, R. 1991, A&A, 246, 249

Pollack, J. B., Hollenbach, D., Beckwith, S., Simonelli, D. P., Roush, T., & Fong, W. 1994, ApJ, 421, 615

Price, S. D., Egan, M. P., Carey, S. J., Mizuno, D. R., & Kuchar, A. 2001, AJ, 121, 2819

Ramesh, B., Bronfman, L., & Deguchi, S. 1997. PASJ 49 (3), 307

Rathborne, J. M., Jackson, J. M., Chambers, E. T., Simon, R., Shipman, R. & Frieswijk, W. 2005, ApJ, 630, L181

Reach, W. T. et al. 2005, PASP, 117, 978

Richards, P. J., Little, L. T., Toriseva, M., & Heaton, B. D. 1987, MNRAS, 228, 43

Rieke, G. H., & Lebofsky, M. J. 1985, ApJ, 288, 618

Rieke, G. H., Young, E. T., Cadien, J., Engelbracht, C. W. et. al. 2004, SPIE, 5487, 50

Robitaille, T. P., Whitney, B. A., Indebetouw, R., Wood, K., & Denzmore, P. 2006, ApJS, 167, 256

Robitaille, T. P., Whitney, B. A., Indebetouw, R., & Wood, K. 2007, ApJS, 169, 32

Sault, R. J., Teuben, P. J., & Wright, M. C. H. 1995, in "Astronomical Data Analysis Software and Systems IV", ed. R. A. Shaw, H. E. Payne, & J. J. E. Hayes, PASP Conf Series 77, 433

Scalise, E., Jr., Rodríguez, L. F. & Mendoza-Torres, E. 1989, A&A, 221, 105

Schutte, A. J., van der Walt, D. J., Gaylard, M. J., & MacLeod, G. C. 1993, MNRAS, 261, 783

Scoville, N. Z., Carlstrom, J. E., Chandler, C. J., Phillips, J. A., Scott, S. L., Tilanus, R. P. J., & Wang, Z. 1993, PASP, 105, 1482

Shepherd, D. S., & Watson, A. M. 2002, ApJ, 566, 966

Shepherd, D. S., Nürnberger, D. E. A., & Bronfman, L. 2004, ApJ, 602, 850 (SNB04)

Shu, F., Tremaine, S., Adams, F., & Ruden, S. 1990, ApJ, 358, 495

Skrutskie, M. F. et al. 2006, AJ, 131, 1163

Smith, H. A., Hora, J. L., Marengo, M., & Pipher, J. L. 2006 ApJ, 645, 1264

Stetson, P. B. 1987, PASP, 99, 191

Szymczak, M., Hrynek, G., & Kus, A. J. 2000, A&AS, 143, 269

Thompson, R. I. 1984, ApJ, 283, 165

Wang, Y., Zhang, Q., Rathborne, J. M., Jackson, J. & Wu, Y. 2006, ApJ, 651, L125

Ward-Thompson, D., André, P., Crutcher, R., Johnstone, D., Onishi, T., Wilson, C. 2007, in Protostars and Planets V, eds. B. Reipurth, D. Jewitt & K. Keil (Tucson: Univ. of Arizona Press), 33

Wilson, T. L. & Rood, R. T. 1994, ARAA, 32, 191

Wood, D. O. S. & Churchwell, E. 1989, ApJS, 69, 831

Zhang, Q., Hunter, T. R., Brand,J., Sridharan, T. K., Cesaroni, R. Molinari, S., Wang, J. & Kramer, M. 2005, ApJ, 625, 864

This preprint was prepared with the AAS LaTeX macros v5.2.

Table 1: G34.4 and G34 MM Outflow Parameters

Source:	G34.4 combined flows	G34 MM combined flows
CO radius of outflow	0.98 pc	0.85 pc
Assumed inclination angle	45°	45°
Outflow Mass† :		
Red-shifted: ^{12}CO	22.6 $M_\odot$	10.6 $M_\odot$
^{13}CO	59.6 $M_\odot$	12.7 $M_\odot$
Blue-shifted: ^{12}CO	14.2 $M_\odot$	1.6 $M_\odot$
^{13}CO	14.8 $M_\odot$	9.9 $M_\odot$
	111.2 $M_\odot$	34.8 $M_\odot$
Momentum	8.3×10^2 $M_\odot$ km s^{-1}	3.5×10^2 $M_\odot$ km s^{-1}
Kinetic Energy	7.8×10^{46} ergs	4.9×10^{46} ergs
Dynamical time scale of CO flow	$\sim 4 \times 10^4$ yr	$\sim 3.8 \times 10^4$ yr
$\dot{M}_f$	1.3×10^{-3} $M_\odot$ yr^{-1}	0.8×10^{-3} $M_\odot$ yr^{-1}
Momentum Supply Rate (Force)	12.2×10^{-3} $M_\odot$ km s^{-1} yr^{-1}	8.0×10^{-3} $M_\odot$ km s^{-1} yr^{-1}
Mechanical Luminosity	11.2 $L_\odot$	9.1 $L_\odot$

† ^{12}CO outflow emission (corrected for optical depth from [CO]/[^{13}CO])
measured between velocities 32.9 to 51.7 km s^{-1} and 63.6 to 77.8 km s^{-1}.
^{13}CO outflow emission (assumed to be optically thin)
measured between velocities 51.7 to 53.6 km s^{-1} and 60.4 to 63.6 km s^{-1}.

Table 2: G34.4 and G34 MM Core Parameters measured from C^{18}O

Source:	G34.4	G34 MM
C^{18}O Core Mass:	692.7 $M_\odot$	75.2 $M_\odot$
v_{LSR}	56.0 km s^{-1}	57.4 km s^{-1}
Momentum	2.0×10^3 $M_\odot$ km s^{-1}	2.5×10^2 $M_\odot$ km s^{-1}
Kinetic Energy	8.0×10^{46} ergs	1.2×10^{46} ergs

Table 3. YSO Cluster Members

Src.[a]	Coordinates		Measured Mid-IR Fluxes and Uncertainties (mJy)											
	α(J2000)	δ(J2000)	F[3.6]	δF[3.6]	F[4.5]	δF[4.5]	F[5.8]	δF[5.8]	F[8.0]	δF[8.0]	F[24]	δF[24][b]	Fit[c]	Reg.[d]
1	$18^h53^m24.999^s$	$1°23'01.4''$	3.43	0.34	2.11	0.23	1.86	0.37	—	—	1.61	0.16	1	S
2	18 53 18.649	1 23 21.8	1.78	0.18	2.01	0.20	2.85	0.28	2.68	0.40	10.54	1.68	1	S
3	18 53 16.833	1 23 26.6	5.20	0.52	6.10	0.61	5.07	0.51	4.33	0.65	6.73	0.67	1	S
4	18 53 19.694	1 23 36.2	6.78	0.68	16.79	1.68	28.13	2.81	20.32	3.05	60.00	U.L.	1	S
5	18 53 17.773	1 23 49.4	8.66	0.87	12.26	1.23	13.92	1.39	15.76	2.36	45.29	4.53	1	S
6	18 53 18.982	1 24 11.5	0.84	0.15	7.66	0.93	5.00	0.86	2.79	0.64	307.85	30.78	1	C
7	18 53 18.825	1 24 19.6	12.22	1.22	26.14	2.61	26.69	2.67	23.15	3.47	150.00	U.L.	1	C
8	18 53 19.404	1 24 24.2	0.25	0.07	1.46	0.16	3.33	0.36	4.18	0.63	150.00	U.L.	1	C
9	18 53 21.127	1 24 27.5	3.79	0.38	3.56	0.36	3.07	0.52	2.00	0.30	19.92	2.54	1	C
10[e]	18 53 18.727	1 24 43.0	5.13	0.92	19.57	1.96	40.99	6.81	59.72	8.96	18,024.00	U.L.	1	C
11[e]	18 53 18.630	1 24 48.3	28.26	7.77	79.15	14.59	168.90	16.89	277.30	45.02	18,024.00	U.L.	1	C
12[f]	18 53 18.058	1 25 25.3	2.24	0.22	16.20	8.00	13.85	1.38	11.34	1.13	8,682.80	868.28	1	C
13	18 53 16.533	1 26 28.6	0.37	0.06	1.03	0.10	1.40	0.22	1.59	0.24	7.11	0.71	1	N
14	18 53 17.321	1 26 33.0	1.88	0.19	2.65	0.27	2.83	0.40	1.77	0.27	15.01	1.50	1	N
15	18 53 17.232	1 26 41.1	5.01	0.50	6.90	0.69	7.18	0.72	6.23	0.93	11.21	1.12	1	N
16	18 53 29.815	1 26 52.7	3.30	0.33	4.12	0.41	4.68	0.53	5.80	0.87	8.09	0.81	1	
17	18 53 21.571	1 26 58.9	0.38	0.06	1.58	0.23	1.58	0.35	—	—	13.46	1.61	1	N
18	18 53 11.979	1 27 09.5	13.41	1.34	10.45	1.04	8.31	0.83	7.87	1.61	119.71	37.16	1	N
19	18 53 17.787	1 27 12.6	0.81	0.09	2.11	0.21	3.29	0.33	3.94	0.59	13.88	1.39	1	N
20	18 53 18.181	1 27 28.5	1.40	0.19	3.23	0.32	3.30	0.41	3.40	0.51	13.21	1.32	1	N
21	18 53 15.807	1 27 37.4	40.59	4.06	41.08	4.11	46.97	4.70	36.85	5.53	20.79	2.08	1	N
22	18 53 18.604	1 27 38.8	0.49	0.09	0.71	0.11	—	—	2.66	0.40	10.97	1.40	1	N
23	18 53 23.391	1 27 57.0	2.47	0.25	2.52	0.25	2.70	0.34	2.35	0.35	4.07	0.41	1	N
24	18 53 23.784	1 28 01.1	0.49	0.08	0.55	0.06	1.02	0.32	0.96	0.14	4.94	0.49	1	N
25	18 53 18.848	1 28 02.7	0.65	0.09	0.58	0.09	—	—	2.59	0.39	—	—	1	N
26	18 53 19.404	1 28 16.1	0.83	0.09	2.12	0.21	2.60	0.42	2.93	0.44	4.16	0.42	1	N
27	18 53 20.005	1 28 19.6	0.55	0.08	1.29	0.23	2.14	0.68	1.47	0.22	29.57	2.96	1	N
28	18 53 19.049	1 28 21.5	2.53	0.29	2.64	0.26	2.23	0.24	1.68	0.25	5.42	0.54	1	N
29	18 53 20.674	1 28 24.1	9.65	0.96	32.79	3.94	26.83	2.68	8.03	1.20	278.27	27.83	1	N
30	18 53 20.078	1 28 43.1	0.27	0.05	1.02	0.11	1.83	0.28	2.49	0.37	15.80	1.58	1	N
31	18 53 18.586	1 25 38.9	0.33	0.08	3.43	0.39	2.50	0.32	1.79	0.27	—	—	2	C
32	18 53 19.144	1 24 35.4	0.68	0.09	1.46	0.18	—	—	—	—	—	—	3	C
33	18 53 13.870	1 26 03.3	0.98	0.13	0.71	0.11	—	—	—	—	3.31	0.59	4	N
34	18 53 13.933	1 24 46.7	—	—	—	—	—	—	—	—	5.79	0.40	4	

Table 3—Continued

Src.[a]	Coordinates α(J2000)	Coordinates δ(J2000)	Measured Mid-IR Fluxes and Uncertainties (mJy) F[3.6]	δF[3.6]	F[4.5]	δF[4.5]	F[5.8]	δF[5.8]	F[8.0]	δF[8.0]	F[24]	δF[24][b]	Fit[c]	Reg.[d]
35	18 53 14.135	1 25 03.8	0.35	0.06	0.34	0.06	—	—	—	—	5.52	1.00	4	
36	18 53 14.702	1 25 25.0	—	—	—	—	—	—	—	—	8.00	0.99	4	
37	18 53 14.884	1 25 49.0	—	—	—	—	—	—	—	—	4.56	0.50	4	
38	18 53 15.298	1 25 48.1	1.27	0.15	0.86	0.09	—	—	—	—	11.14	1.11	4	
39	18 53 15.562	1 23 25.2	—	—	—	—	—	—	—	—	2.75	0.53	4	S
40	18 53 16.029	1 24 25.4	—	—	—	—	—	—	—	—	21.63	1.27	4	C
41	18 53 16.811	1 24 11.9	—	—	—	—	—	—	—	—	10.22	0.47	4	C
42	18 53 16.908	1 26 32.0	—	—	—	—	—	—	—	—	8.87	0.92	4	N
43	18 53 18.026	1 26 25.9	—	—	—	—	—	—	—	—	42.84	2.55	4	N
44	18 53 18.065	1 23 24.8	—	—	—	—	—	—	—	—	7.76	0.97	4	S
45	18 53 18.085	1 26 12.0	0.49	0.07	0.45	0.08	—	—	—	—	8.27	3.97	4	N
46	18 53 18.409	1 23 38.7	—	—	—	—	—	—	—	—	10.10	0.83	4	S
47	18 53 18.516	1 23 56.8	—	—	—	—	—	—	—	—	17.53	4.67	4	C
48	18 53 18.589	1 26 49.5	—	—	—	—	—	—	—	—	4.47	0.50	4	N
49	18 53 18.600	1 23 46.2	—	—	—	—	—	—	—	—	20.59	2.42	4	S
50	18 53 19.904	1 28 08.6	—	—	0.68	0.08	1.30	0.36	—	—	12.96	1.30	4	N
51	18 53 21.233	1 25 12.2	—	—	—	—	—	—	—	—	14.51	0.83	4	C
52	18 53 22.760	1 22 30.3	—	—	—	—	—	—	—	—	6.44	0.95	4	S
53	18 53 22.826	1 25 10.0	0.80	0.10	0.67	0.10	—	—	—	—	35.49	U.L.	4	
54	18 53 22.905	1 25 07.0	1.58	0.16	1.53	0.18	—	—	—	—	35.49	U.L.	4	

[a]Sources are grouped in order of Fit flag, and then listed in order of increasing declination.

[b]Where 2 or more GLIMPSE sources are confused with a single MIPS source, we treat the 24 μm flux as an upper limit (U.L) only.

[c]The Fit flags are designated as follows:
1 = Source well-fit as a YSO, meeting the $\chi^2/N_{\rm data} \leq 4.8$ criterion discussed in the text.
2 = Fit failed to meet the χ^2 criterion, but source is considered to be a probable YSO based upon visual inspection of its mid-IR SED.
3 = Not able to fit because source is detected only in the GLIMPSE [3.6] & [4.5] bands (includes the possible source of Outflow G34.4:D).
4 = MIPS 24-μm-detected source not fittable because it is detected in fewer than 3 of the IRAC+2MASS bands. The majority of these sources are probably YSOs due to their location near the IR dark cloud, but a few could be field stars on the asymptotic giant branch.

[d]Region of Figure 11 in which the source is located. Region C refers to the central part of the IR dark cloud containing the OVRO observations. Region N represents the dark cloud north of C, while Region S represents the dark cloud south of C. Unlabeled sources lie outside of these 3 regions.

[e]These sources overlie the UC HII region, which produces bright diffuse emission in all 4 *MSX* bands as well as at MIPS 24 μm and 70 μm. Although

these YSOs may be bright enough to be detected by *MSX* and MIPS, they are confused with the UC HII.

[f]The IR counterpart to G34.4 MM. It is detected also by *MSX* at 21.3 μm and by MIPS at 70 μm, with fluxes of 4,900±258 and 322,000±128,000 mJy, respectively.

Table 4. YSO Model Parameters[a] from SED Fits to Cluster Members

Src.	Fit	χ^2_{min}	χ^2_{max}[b]	# Fits	A_V	$M_\star$ ($M_\odot$)	$L_\star$ ($L_\odot$)	$\dot{M}_{\rm env}$ ($M_\odot$ yr^{-1})[c]	i
1	1	7.63	13.57	112	8.5 – 15.1	2.63E+00 – 4.34E+00	3.44E+01 – 2.83E+02	0	18.2 – 87.1
2	1	1.82	7.81	322	1.5 – 24.7	5.81E-01 – 3.95E+00	6.22E+00 – 4.11E+01	0 – 3.44E-05	18.2 – 81.4
3	1	8.24	14.21	96	11.4 – 22.8	2.65E+00 – 4.24E+00	4.82E+01 – 1.18E+02	0 – 3.06E-07	41.4 – 81.4
4	1	8.18	12.08	29	22.5 – 58.3	1.03E+00 – 6.77E+00	1.10E+02 – 1.54E+03	0	18.2 – 81.4
5	1	0.86	7.85	185	11.4 – 26.5	3.32E+00 – 5.03E+00	1.03E+02 – 3.86E+02	0 – 8.44E-06	18.2 – 81.4
6	1	5.16	11.15	53	0.0 – 6.9	2.41E+00 – 6.59E+00	8.22E+01 – 3.40E+02	5.36E-05 – 1.10E-03	31.8 – 69.5
7	1	1.43	5.40	106	16.7 – 38.1	3.71E+00 – 6.10E+00	1.82E+02 – 9.68E+02	0 – 1.60E-06	41.4 – 81.4
8	1	2.83	6.82	323	0.0 – 59.9	1.94E-01 – 5.18E+00	4.75E+00 – 2.27E+02	0 – 4.22E-04	18.2 – 75.5
9	1	6.46	12.42	36	0.0 – 13.2	9.22E-01 – 3.34E+00	9.97E+00 – 3.53E+01	1.18E-06 – 9.78E-05	49.5 – 81.4
10	1	0.69	4.69	846	0.0 – 60.0	5.00E-01 – 9.97E+00	4.47E+01 – 4.46E+03	0 – 1.04E-03	18.2 – 81.4
11	1	0.17	5.17	879	5.2 – 50.2	2.13E+00 – 9.92E+00	2.12E+02 – 5.16E+03	0 – 2.18E-03	18.2 – 81.4
12[d]	1	6.62	36.13	10	38.8 – 41.5	1.36E+01 – 1.39E+01	6.92E+03 – 9.39E+03	5.91E-04 – 9.96E-04	56.6
13	1	3.11	8.11	200	7.5 – 60.0	9.65E-01 – 4.25E+00	1.12E+01 – 1.49E+02	0 – 1.01E-04	18.2 – 87.1
14	1	1.57	6.36	31	0.0 – 18.7	4.33E-01 – 2.70E+00	5.32E+00 – 3.16E+01	7.22E-06 – 1.10E-04	41.4 – 81.4
15	1	0.78	5.77	186	0.0 – 25.5	1.46E+00 – 4.40E+00	1.95E+01 – 1.49E+02	0 – 1.73E-05	18.2 – 81.4
16	1	0.03	5.02	697	0.0 – 30.4	2.17E+00 – 4.24E+00	1.67E+01 – 1.97E+02	0 – 6.68E-07	18.2 – 81.4
17	1	7.49	11.49	470	15.8 – 60.0	2.04E+00 – 5.44E+00	2.89E+01 – 6.58E+02	0 – 1.09E-07	18.2 – 87.1
18	1	6.78	14.64	19	0.0 – 9.4	3.60E+00 – 5.64E+00	1.10E+02 – 1.66E+02	2.74E-05 – 9.41E-04	18.2 – 69.5
19	1	1.19	6.18	209	19.4 – 60.0	2.65E+00 – 4.46E+00	2.89E+01 – 3.14E+02	0 – 2.82E-08	18.2 – 81.4
20	1	4.89	11.30	14	0.0 – 7.1	6.60E-01 – 1.54E+00	4.82E+00 – 1.44E+01	0 – 8.48E-06	18.2 – 81.4
21	1	18.30	26.23	14	17.5 – 19.1	6.14E+00 – 6.63E+00	9.96E+02 – 1.34E+03	0	18.2 – 87.1
22	1	0.01	4.01	425	1.5 – 60.0	4.18E-01 – 4.71E+00	5.00E+00 – 3.18E+02	0 – 1.09E-04	18.2 – 81.4
23	1	1.72	8.72	165	0.0 – 21.0	1.00E+00 – 3.83E+00	1.04E+01 – 5.35E+01	0 – 1.88E-05	18.2 – 81.4
24	1	0.62	5.62	1070	0.0 – 45.6	1.80E-01 – 3.73E+00	1.44E+00 – 5.09E+01	0 – 2.99E-05	18.2 – 81.4
25	1	0.24	4.23	22	6.7 – 10.5	1.89E+00 – 2.77E+00	1.25E+01 – 7.58E+01	0	18.2 – 87.1
26	1	0.02	3.98	221	18.6 – 54.0	2.05E+00 – 3.99E+00	1.67E+01 – 2.05E+02	0	18.2 – 87.1
27	1	0.39	5.38	293	0.0 – 52.3	4.14E-01 – 5.03E+00	5.29E+00 – 1.12E+02	2.95E-06 – 3.31E-04	31.8 – 81.4
28	1	3.85	11.84	98	3.6 – 14.5	7.91E-01 – 3.64E+00	6.74E+00 – 3.20E+01	0 – 1.86E-05	41.4 – 81.4

Table 4—Continued

Src.	Fit	χ^2_{min}	χ^2_{max} [b]	# Fits	A_V	$M_\star$ ($M_\odot$)	$L_\star$ ($L_\odot$)	$\dot{M}_{\rm env}$ ($M_\odot$ yr^{-1})[c]	i
29	1	17.39	21.98	7	3.9 – 17.8	4.84E+00 – 6.80E+00	1.69E+02 – 3.42E+02	6.03E-05 – 2.10E-04	41.4 – 75.5
30	1	3.54	8.54	186	1.4 – 60.0	1.49E-01 – 4.71E+00	1.99E+00 – 2.92E+02	0 – 1.71E-04	18.2 – 81.4
31	2	39.45	51.32	19	7.4 – 40.5	7.51E+00 – 1.34E+01	1.02E+03 – 3.84E+03	2.67E-04 – 2.21E-03	31.8 – 87.1

[a]The range of values reported here for each YSO parameter has a 95% probability, based on the probability distribution of best fits, of containing the actual value of that parameter for each source.

[b]Fits having $\chi^2 \leq \chi^2_{\rm max}$ are used in computing the probability distribution of YSO parameters. For each source, $\chi^2_{\rm max} - \chi^2_{\rm min} = \Delta N_{\rm data}$, where $N_{\rm data}$ is the number of flux data points used in the fit and $\Delta = 1$ for Fit=1, $\Delta = 3$ for Fit=2.

[c]For models with $\dot{M}_{\rm env} < 10^{-9}$ $M_\odot$ yr^{-1}, the envelope accretion rate is considered to be zero.

[d]For this source, the IR counterpart to G34MM, we report the probability distribution of parameters from the 10 best fits.

Figure Captions

Figure 1. Four-color GLIMPSE image showing 3.6 μm, 4.6 μm, 5.8 μm, and 8.0 μm as blue, green, orange, and red colors, respectively. The image is displayed in galactic coordinates and is roughly $16.6' \times 21.5'$ in size. The white box at upper left gives the field of view shown in Figure 2. The G34.4 UC HII region is in the center of the box within a dense cloud filament seen as a dark lane. The mid-IR counterpart to the G34.4 MM core is seen as a faint green smudge immediately to the upper left of the UC HII region. The larger nebula in the lower right of the image is associated with the cometary UC HII region G34.26. The bright green emission emanating from this region traces a very energetic outflow. This GLIMPSE image includes the same data as reported in Rathborne et al. (2005) but it covers a wider field-of-view to show the physical relationship between the IR-dark cloud in which the G34.4 UC HII is located and the HII region G34.26.

Figure 2. Four images, all showing the same field of view. Clockwise from the upper-left panel are: (a) 2MASS K-band, (b) GLIMPSE 4.5 μm, (c) GLIMPSE 8.0 μm, and (d) a 3-color image combining the three other images as blue, green, and red, respectively. Green plus signs mark the positions of the UC HII and G34.4 MM, while green circles show the locations predicted for the driving sources of outflows G34.4:D and G34.4:E. The white box gives the approximate field of view of Figure 3. The locations of the millimeter cores detected by Rathborne et al. (2005) in J2000 coordinates are: MM1: $18^h53^m18.0^s$, $01°25'24''$; MM3: $18^h53^m20.4^s$, $01°28'23''$; MM4: $18^h53^m19.0^s$, $01°24'08''$;

Figure 3. CO(J=1−0) red and blue-shifted emission. Top left panel shows red and blue-shifted emission from 62.3 to 79.2 km s^{-1} and 37.5 to 53.2 km s^{-1}, respectively. The RMS is 470 mJy beam^{-1} km s^{-1} in the red-shifted image and 370 mJy beam^{-1} km s^{-1} in the blue-shifted image. Bottom panels show low-velocity CO emission (left panel, 62.3 to 67.5 km s^{-1} and 49.3 to 53.2 km s^{-1}, RMS = 350 mJy beam^{-1} km s^{-1}) and higher velocity CO emission (right panel, 67.5 to 79.2 km s^{-1} and 37.5 to 49.3 km s^{-1}, RMS = 350 mJy beam^{-1} km s^{-1}). In all contour maps, contours are plotted at $3, 4, 5, 7, 10, 15, 20\,\sigma$ and continue with a spacing of 5σ. The top right panel shows the NIR K band image of Shepherd et al. (2004) with the locations of the proposed outflows overlaid. In all panels: the solid circle represents the location of G34.4 MM, the star shows the location of the UC HII region, the outflow (A) from G34.4 MM is outlined with a series of arcs which delineate the approximate boundaries of the flow. Four other proposed outflows are shown as arrows. A solid triangle indicates the possible location of the driving source of an outflow. The outflow from the UC HII region is one-sided since only the blue-shifted outflow is clearly detected. The synthesized beam of $3.83'' \times 3.45''$ at P.A. –59.7° is shown in the bottom right of the upper left panel.

Figure 4. $C^{18}O$ (top, left panel) and ^{13}CO (top, center panel) integrated emission

(moment 0) from 62.1 km s^{-1} to 54.6 km s^{-1} and 64.5 km s^{-1} to 49.5 km s^{-1}, respectively (v_{LSR} = 57 km s^{-1}). The RMS in the C^{18}O image is 200 mJy beam^{-1} km s^{-1}; contours are plotted at $3, 5, 7, 9, 11, 13, 15, \&17\sigma$ while grey scale is shown from 200 mJy beam^{-1} km s^{-1} to a peak of 3.1 Jy beam^{-1} km s^{-1}. The RMS in the ^{13}CO image is 280 mJy beam^{-1} km s^{-1}; contours are plotted at $3, 5, 7, 9, 12, 15, 20, 25, \& 30\sigma$ while grey scale is shown from 280 mJy beam^{-1} km s^{-1} to a peak of 9.0 Jy beam^{-1} km s^{-1}. Plus symbols represent the locations of the UC HII region and G34.4 MM. Green triangles represent the locations of spectra taken for optical depth estimates in the outflows. A scale size of 0.55 is shown in the left panel, synthesized beams are shown in the bottom right of each panel. The top, right panel shows ^{13}CO red and blue-shifted emission from 63.1 to 61.8 km s^{-1} and 52.3 to 49.5 km s^{-1}, respectively. The RMS in the image is 100 mJy beam^{-1} km s^{-1}. Contours are plotted at $3, 6, 9, 12, 15, 18$ and $21\,\sigma$. Symbols are the same as in Figure 3. The bottom two panels show moment 1 maps of C^{18}O & ^{13}CO in which the brightness of the color is proportional to the intensity in the moment 0 image. Color bars show velocity and brightness scales in each image.

Figure 5. CO(J=1−0) channel maps at 1.3 km s^{-1} spectral resolution. The central velocity is indicated in the upper left of each panel. The channel RMS is 60 mJy beam^{-1}, the peak is 3.3 Jy beam^{-1}, and contours are plotted at $\pm5, 15, 20, 30, 40$ and $50\,\sigma$. The lower right panel shows the synthesized beam in the bottom right corner ($3.83'' \times 3.45''$ at P.A. $-59.7°$) and a scale size of 0.55 pc. Plus symbols represent the locations of the UC HII region at the 6 cm continuum peak and G34.4 MM as indicated in the upper left panel.

Figure 6. ^{13}CO(J=1−0) channel maps at 1.36 km s^{-1} spectral resolution. The central velocity is indicated in the upper left of each panel. The channel RMS is 44 mJy beam^{-1}, the peak is 1.7 Jy beam^{-1}, and contours are plotted at $\pm3, 5, 7, 9, 12, 15, 20$ and $25\,\sigma$. The lower right panel shows the synthesized beam in the bottom right corner ($4.04'' \times 3.83''$ at P.A. $-49.9°$) and a scale size of 0.55 pc. Plus symbols represent the locations of the UC HII region at the 6 cm continuum peak and G34.4 MM as indicated in the upper left panel.

Figure 7. C^{18}O(J=1−0) channel maps at 0.7 km s^{-1} spectral resolution. The central velocity is indicated in the upper left of each panel. The channel RMS is 60 mJy beam^{-1}, the peak is 0.92 Jy beam^{-1}, and contours are plotted at $\pm3, 5, 7, 9, 11, 13$ and $15\,\sigma$. The lower right panel shows the synthesized beam in the bottom right corner ($4.04'' \times 3.83''$ at P.A. $-50.1°$) and a scale size of 0.55 pc. Plus symbols represent the locations of the UC HII region at the 6 cm continuum peak and G34.4 MM as indicated in the upper left panel.

Figure 8. Spectra convolved with a $10''$ beam taken in CO, ^{13}CO and C^{18}O at different locations in the image. The ratio of the CO and ^{13}CO emission was used to calculate optical depth in the red and blue-shifted outflow lobes as indicated by the dashed-dot lines and

arrows in the figure. Panels i) & ii) show spectra taken near the G34.4 UC HII region at positions $18^h53^m18.320^s$ $1°24'45.84''$ and $18^h53^m19.203^s$ $1°24'39.38''$, respectively. Panels iii) & iv) show spectra taken near the G34 MM core at positions $18^h53^m18.065^s$ $1°25'25.06''$ and $18^h53^m17.284^s$ $1°25'13.52''$, respectively. The locations of the spectra relative to the ^{13}CO emission is shown in the center panel of Figure 4. The dashed vertical line at 57 km s^{-1} helps to illustrate that the peak of the C^{18}O line shifts from 57.4 km s^{-1} toward the G34 MM core to 56 km s^{-1} toward the G34.4 UC HII region core.

Figure 9. GLIMPSE 4.5 μm image in inverted greyscale showing locations of G34.4 MM and G34.4 UC HII region as crosses. Open diamonds show the predicted locations of the driving sources of outflows G34.4:D and E based on CO and ^{13}CO morphology. GLIMPSE sources are located very near the predicted positions suggesting that GLIMPSE has detected two sources driving outflows D and E. ^{13}CO red- and blue-shifted emission contours from Fig. 4 are overlaid for reference.

Figure 10. GLIMPSE and MIPSGAL 3-color image with 4.5 μm (blue), 8.0 μm (green) and 24 μm (red). The probable YSO cluster members listed in Table 3 are marked by color-coded circles: green = good YSO fits ($\chi^2/N_{\rm data} \leq 4.8$), yellow = bad YSO fits ($\chi^2/N_{\rm data} > 14.8$), cyan = source detected in fewer than four bands, and green = MIPS 24 μm point sources detected in too few IRAC+2MASS bands to be fit. Sources well-fit by stellar photospheres are marked by blue circles. The IR dark cloud has been divided into 3 regions for the purpose of the YSO census: Region C (large white circle) contains the OVRO observations and regions N and S are (large white rectangles) are the portions of the dark cloud lying to the north and south, respectively, of region C. Source numbers from Table 3 for the YSOs discussed in Section 3.4 are also shown.

Figure 11: (a) Ten best YSO SED model fits to the IR fluxes of source 12/G34.4 MM. The fitting assumes that the mid-IR flux from the millimeter core is dominated by a single source. The [4.5] upper limit (inverted triangle) was used because the source appears to have excess flux in this bandpass due to molecular emission associated with outflow activity that has not been incorporated into the YSO models. The thickest line represents the best fit to the data, and different colors represent the SED observed through different apertures, from smallest (IRAC, black) to largest (*MSX* 21.3 μm, green). The dashed line shows the photospheric flux from the best-fit YSO model, as it would appear if suffering from interstellar extinction only in the absence of circumstellar material. (b) Masses and luminosities of the best fit models. The shaded contour regions represent the logarithmic density of models in the mass-luminosity parameter space. The darkest gray represents a model density 1000 times higher than that of the lightest grey. The white region beyond the lowest contour shows the part of parameter space that lies beyond the edge of the model grid.

Figure 12: (a) Same as Figure 11a, but for the other 6 well-fit YSOs in region C. All fits used to compute the model parameter ranges in Table 4 are plotted. Sources 10 and 11 overlap the UC HII region, and hence the diffuse mid-IR fluxes associated with the UC HII region in all 4 *MSX* bands and MIPS 24 and 70 μm were used as upper limits to the fits. (b) Same as Figure 11b, but for the 6 well-fit YSOs plotted in Figure 12a.

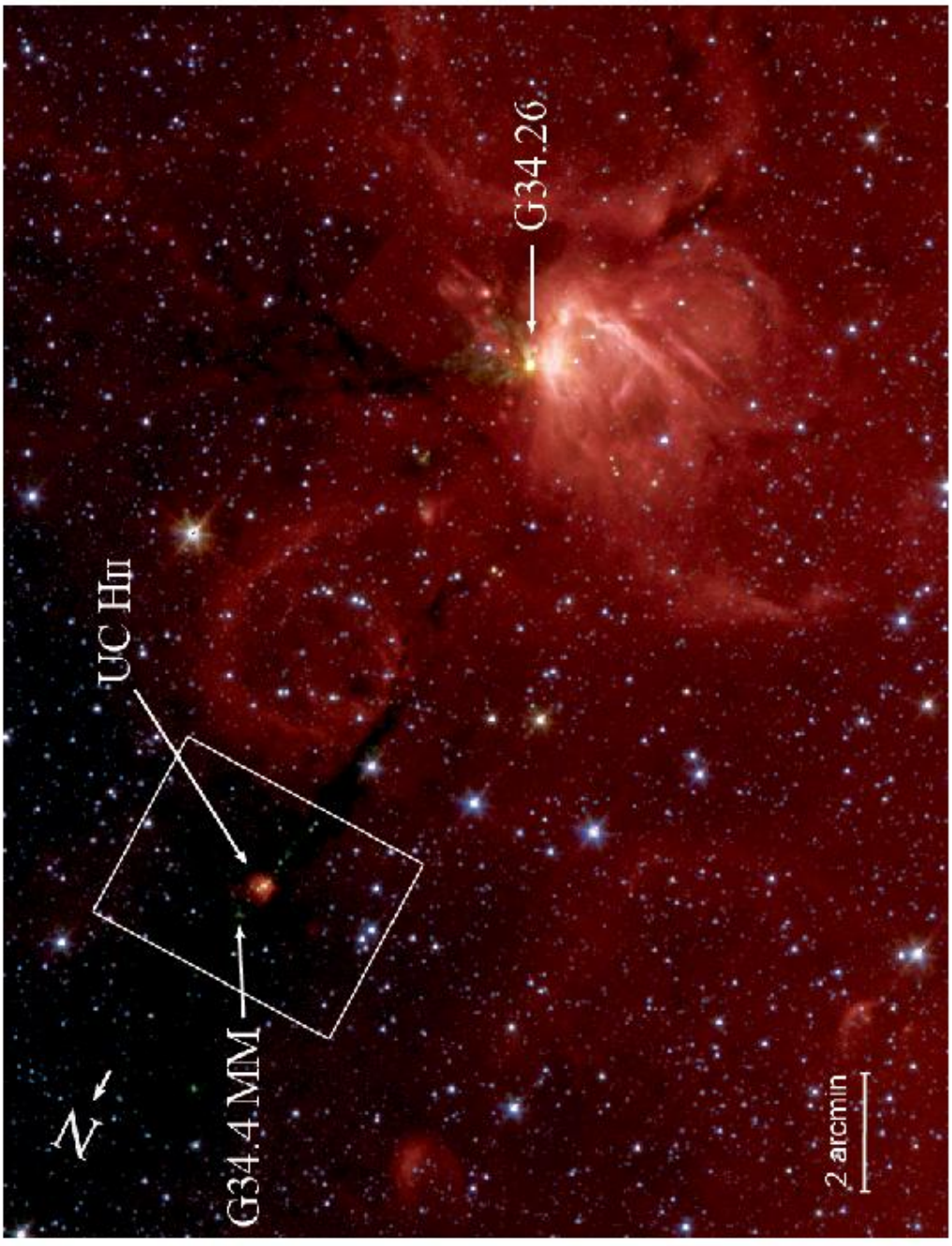

Figure 1.

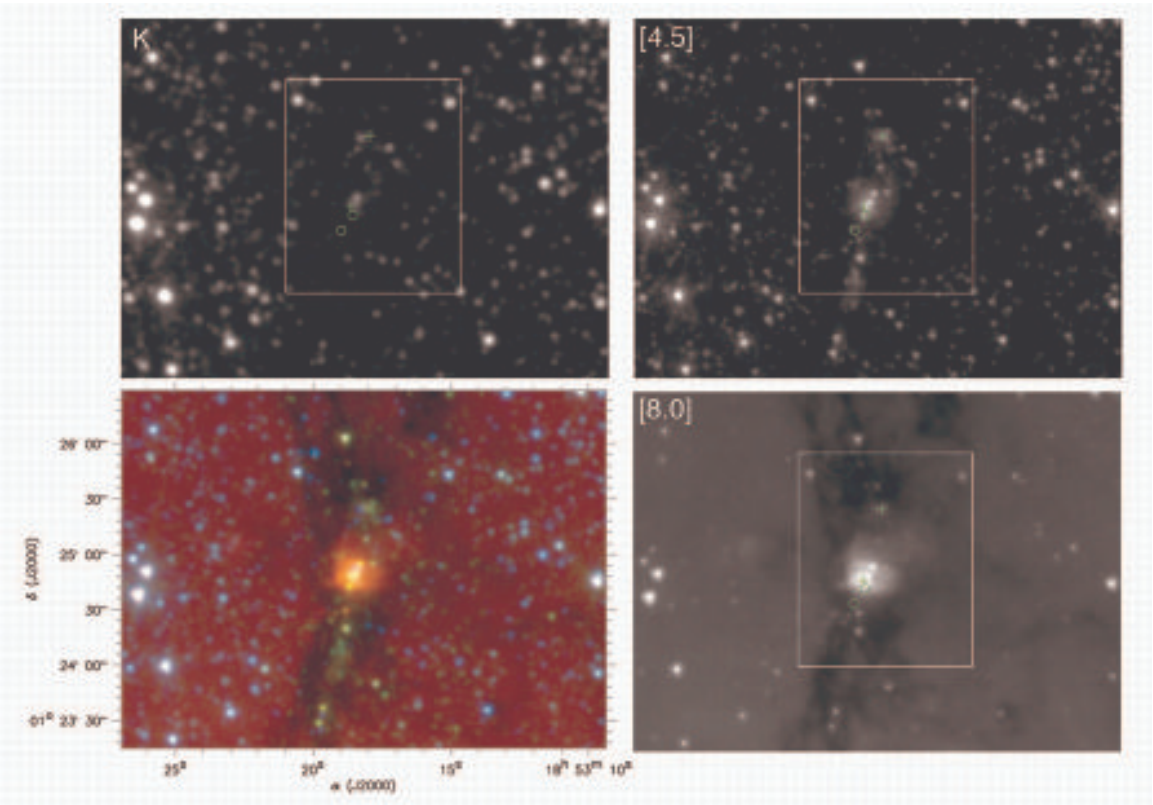
K
[4.5]
[8.0]
26' 00"
30"
25' 00"
30"
24' 00"
01h 23' 30"
δ (J2000)
25s
20s
15s
18h 53m 10s
α (J2000)

Figure 2.

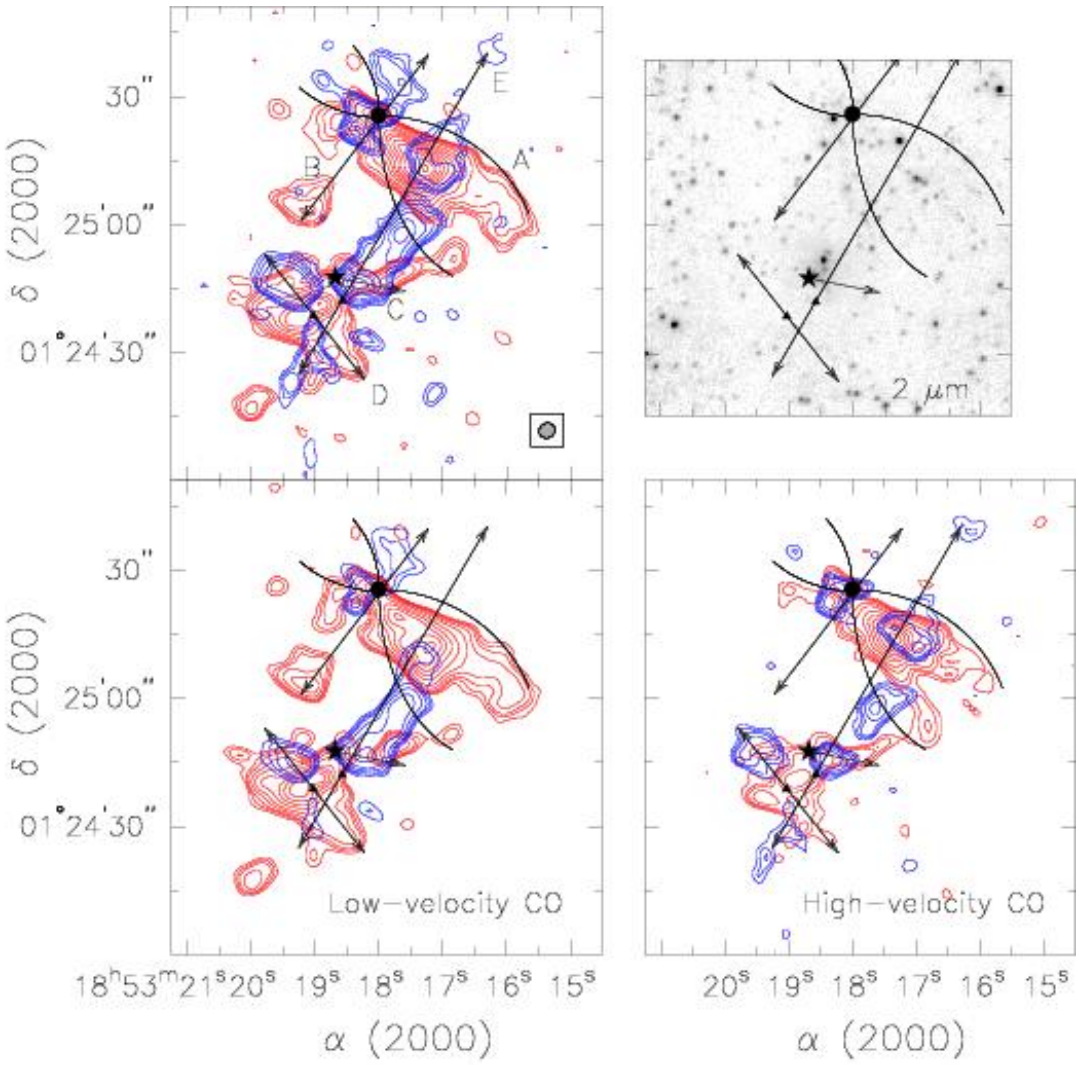
30"
25'00"
01°24'30"
δ (2000)
E
A
B
C
D
2 μm
Low−velocity CO
High−velocity CO
18h53m21s20s 19s 18s 17s 16s 15s
20s 19s 18s 17s 16s 15s
α (2000)

Figure 3.

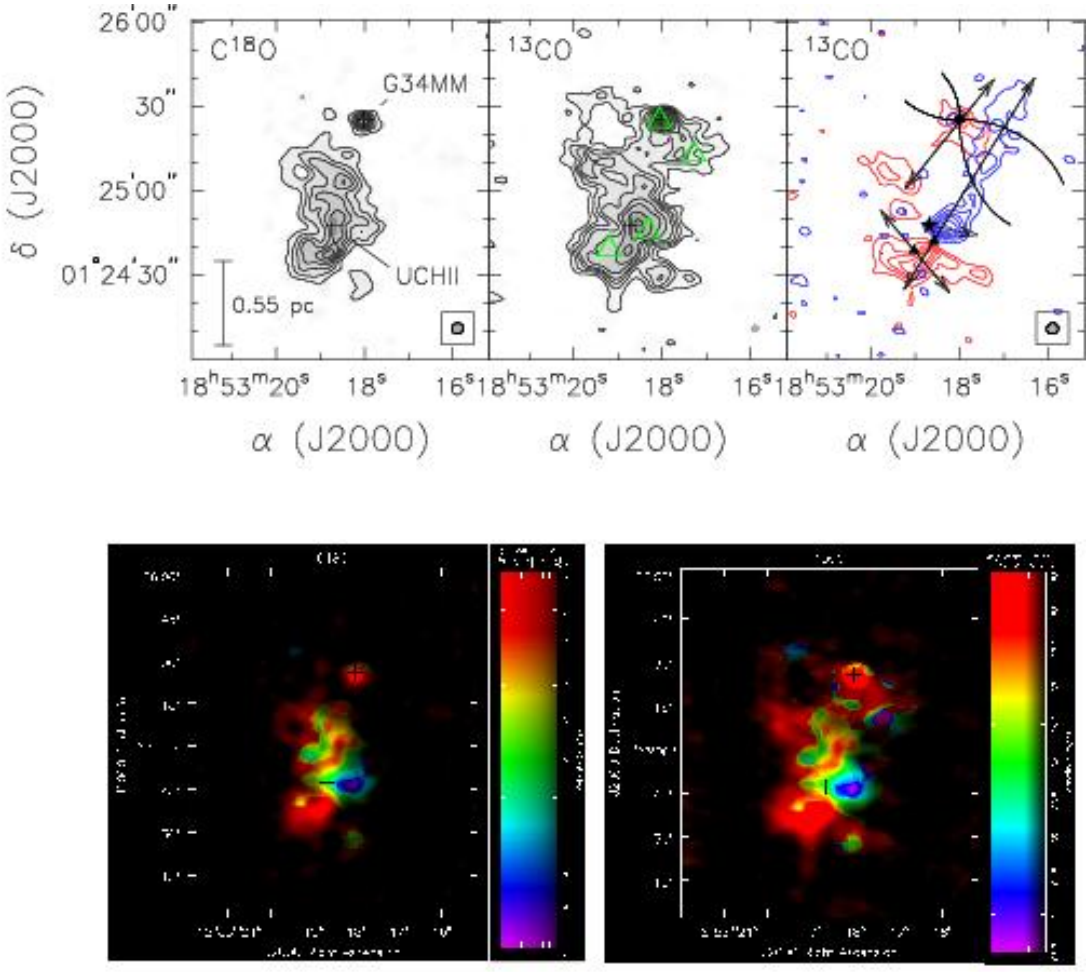
C18O
13CO
13CO
G34MM
UCHII
0.55 pc
26'00"
30"
25'00"
01°24'30"
δ (J2000)
18h53m20s
18s
16s
α (J2000)

Figure 4.

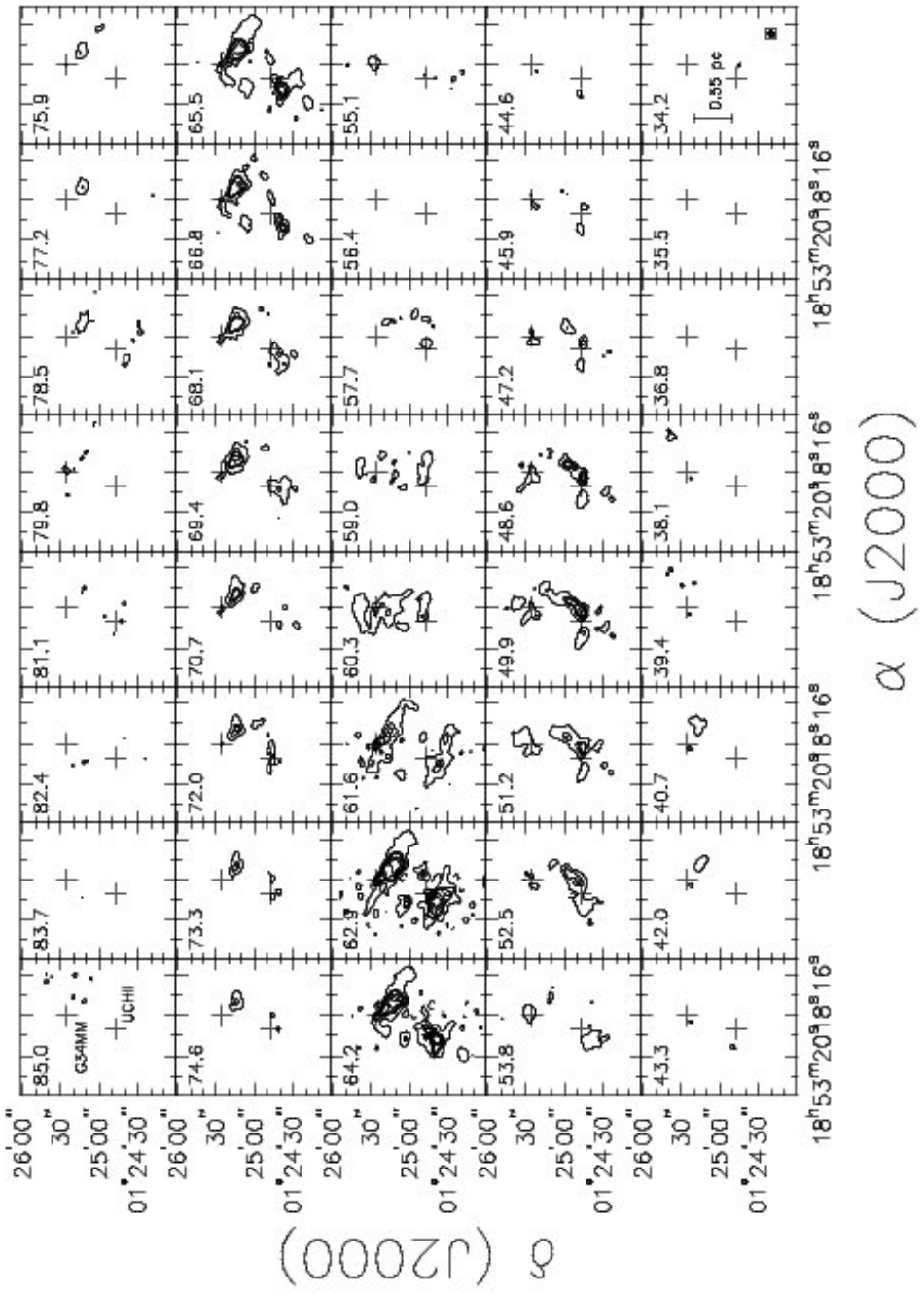

Figure 5.

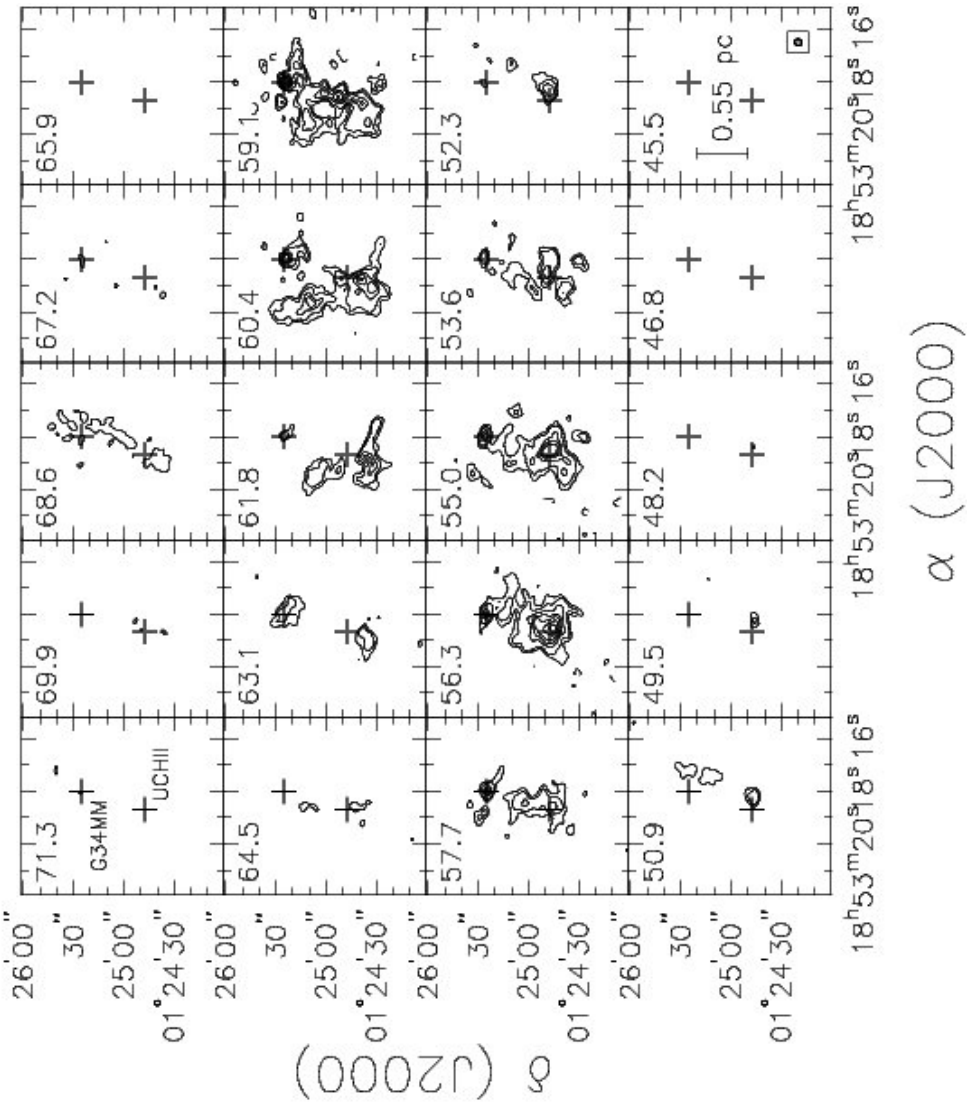
71.3
G34MM
UCHII
69.9
68.6
67.2
65.9
64.5
63.1
61.8
60.4
59.1
57.7
56.3
55.0
53.6
52.3
50.9
49.5
48.2
46.8
45.5
0.55 pc
26'00"
30"
25'00"
01°24'30"
δ (J2000)
18h53m20s18s16s
α (J2000)

Figure 6.

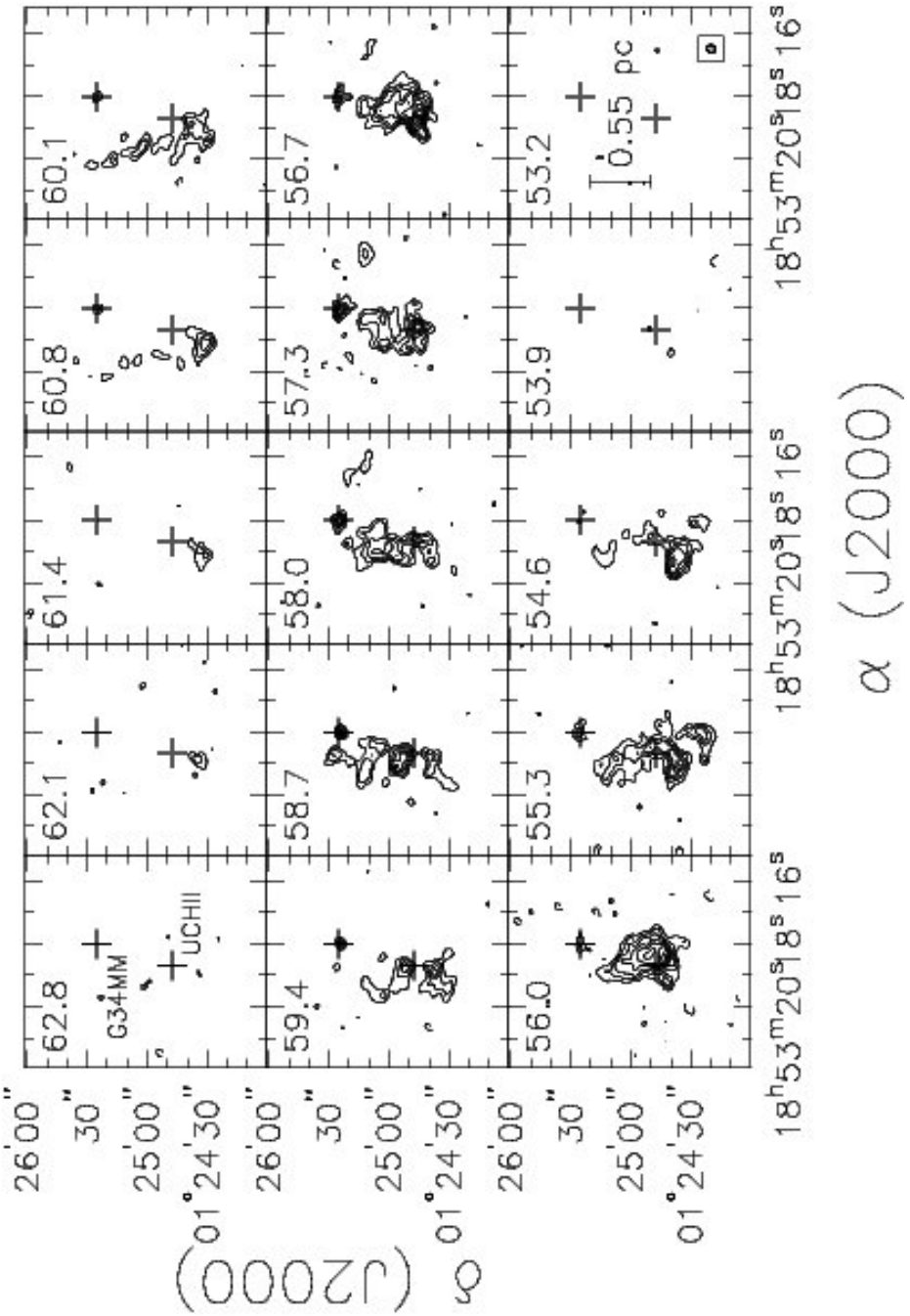
62.8
G34MM
UCHII
62.1
61.4
60.8
60.1
59.4
58.7
58.0
57.3
56.7
56.0
55.3
54.6
53.9
53.2
0.55 pc
26'00"
30"
25'00"
01°24'30"
δ (J2000)
18h53m20s18s16s
α (J2000)

Figure 7.

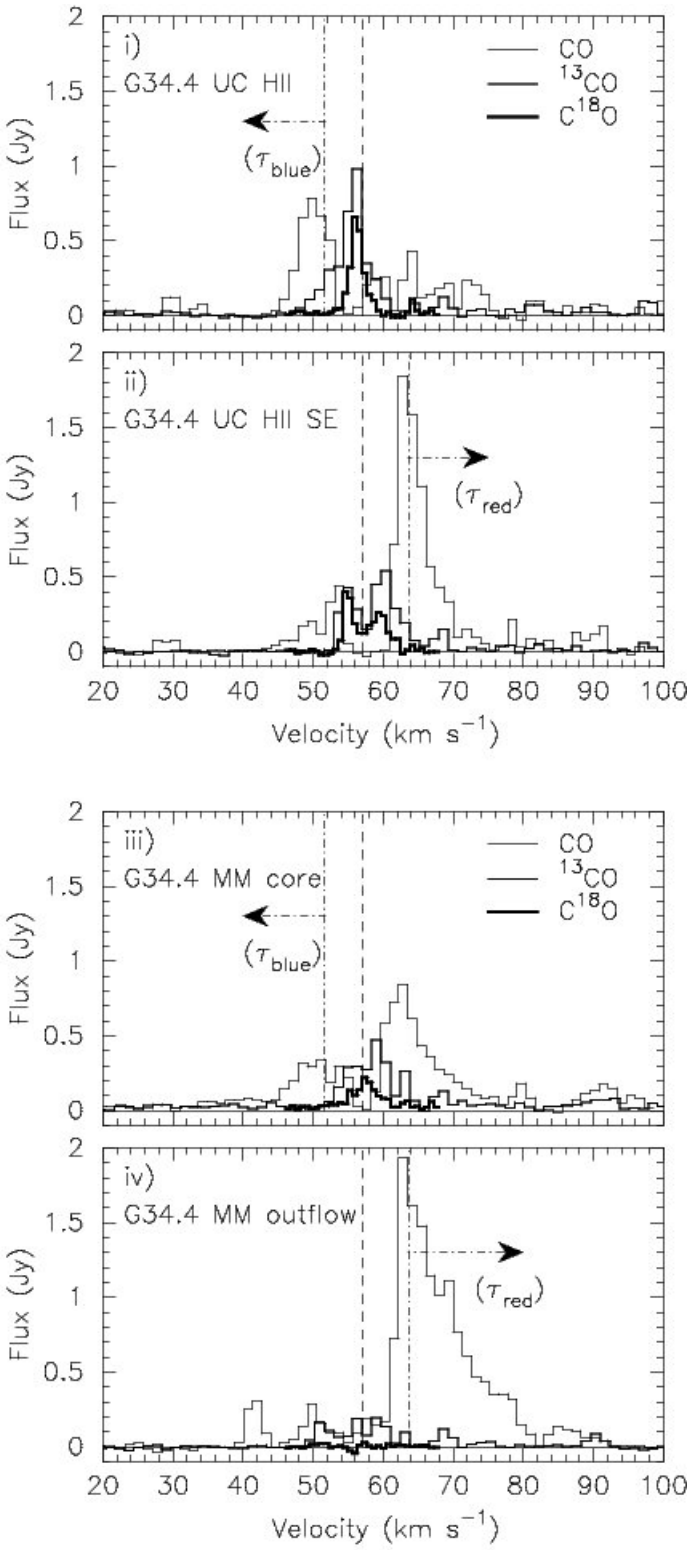
i)
G34.4 UC HII
CO
^{13}CO
C^{18}O
(τ_{blue})
ii)
G34.4 UC HII SE
(τ_{red})
iii)
G34.4 MM core
(τ_{blue})
iv)
G34.4 MM outflow
(τ_{red})
Flux (Jy)
Velocity (km s^{-1})

Figure 8.

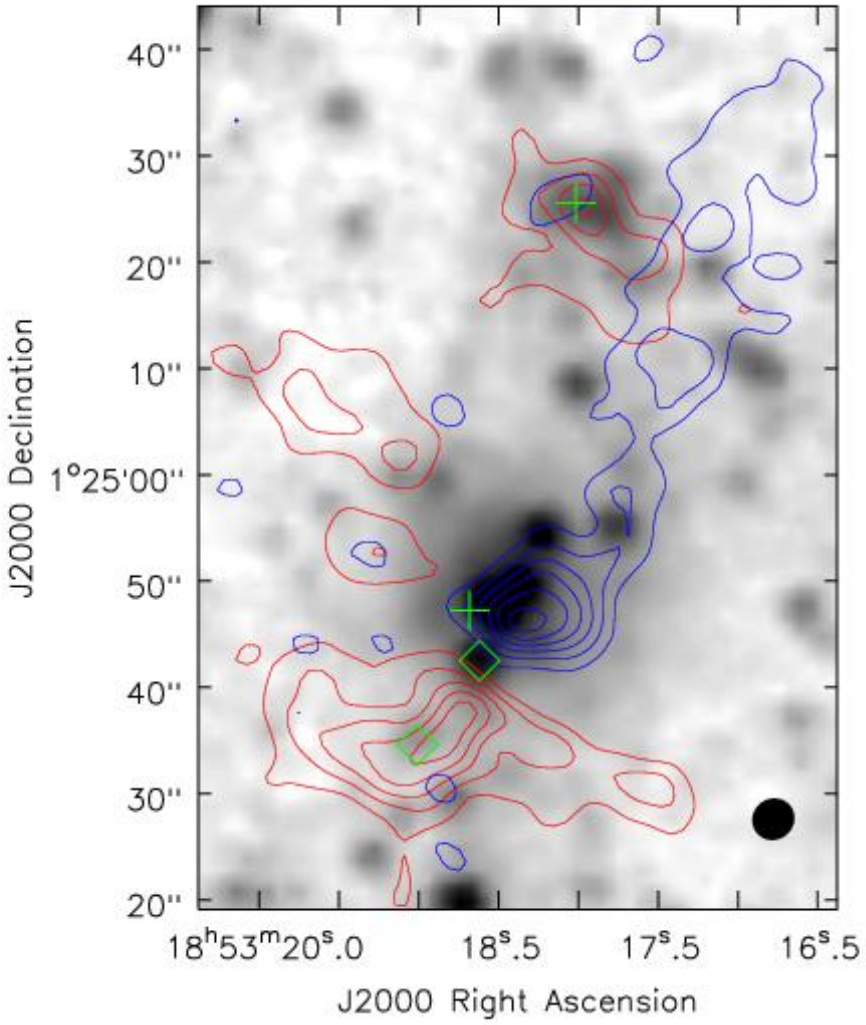
40''
30''
20''
10''
1°25'00''
50''
40''
30''
20''
J2000 Declination
18h53m20s.0
18s.5
17s.5
16s.5
J2000 Right Ascension

Figure 9.

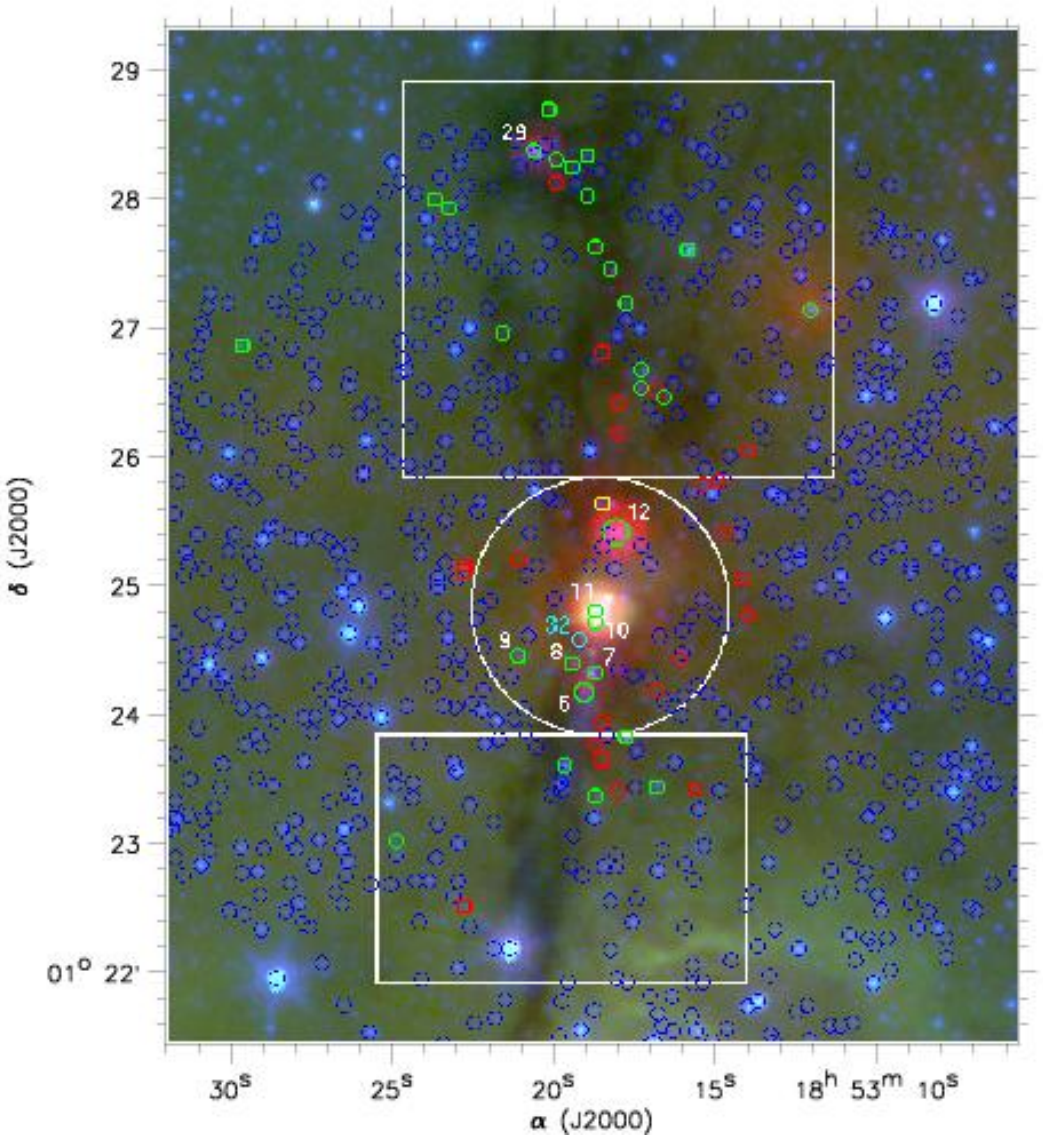
29
28
27
26
25
24
23
01° 22'
δ (J2000)
30s
25s
20s
15s
18h 53m 10s
α (J2000)
29
12
11
32
10
9
8
7
6

Figure 10.

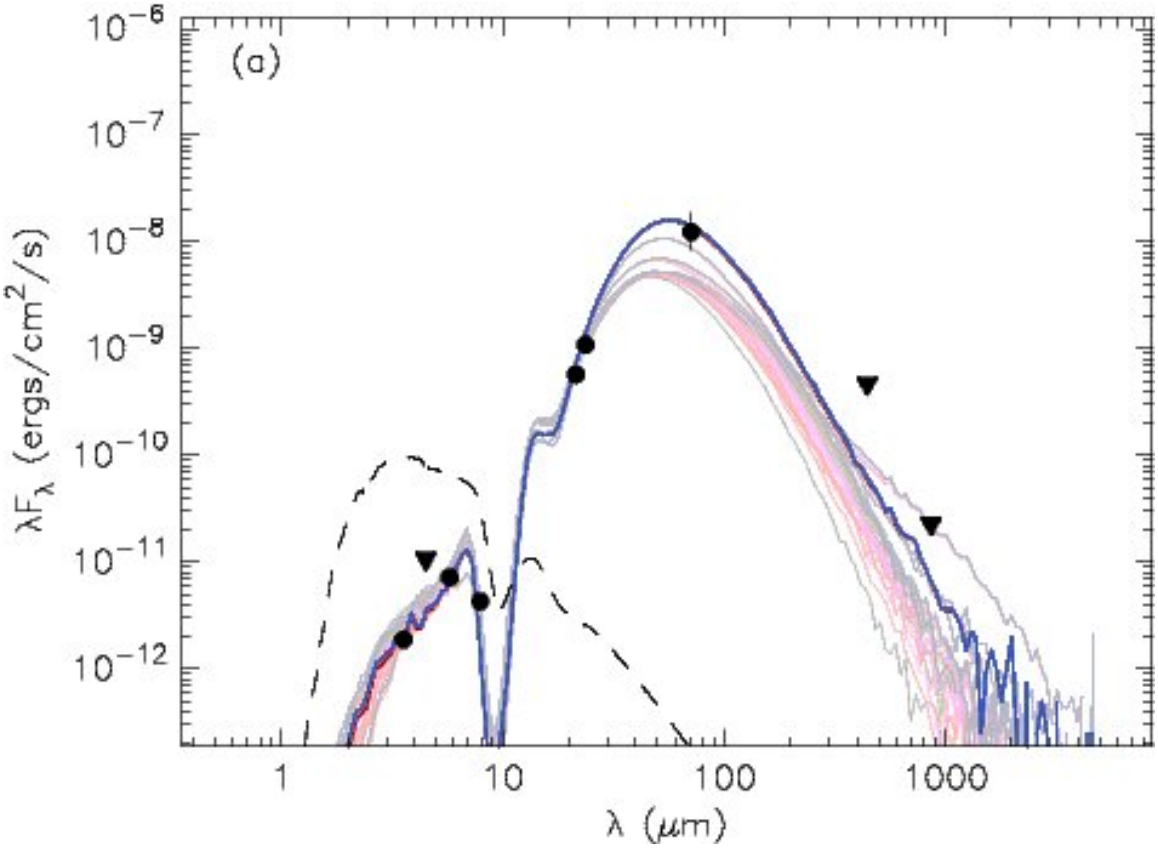
(a)
10^{-6}
10^{-7}
10^{-8}
10^{-9}
10^{-10}
10^{-11}
10^{-12}
λF_λ (ergs/cm^2/s)
1
10
100
1000
λ (μm)

Figure 11a.

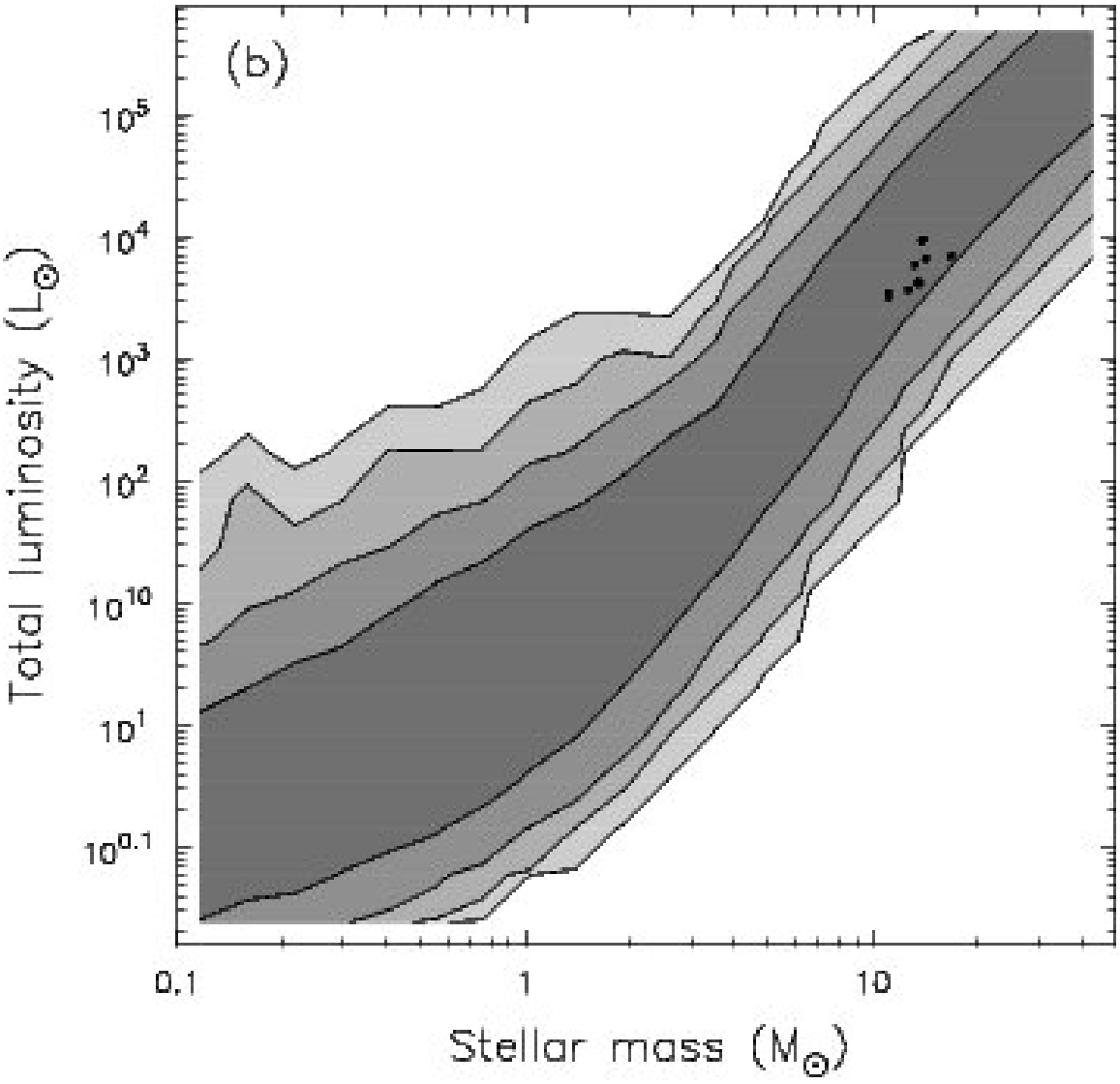
(b)
Total luminosity ($L_\odot$)
10^5
10^4
10^3
10^2
10^{10}
10^1
$10^{0.1}$
0.1
1
10
Stellar mass ($M_\odot$)

Figure 11b.

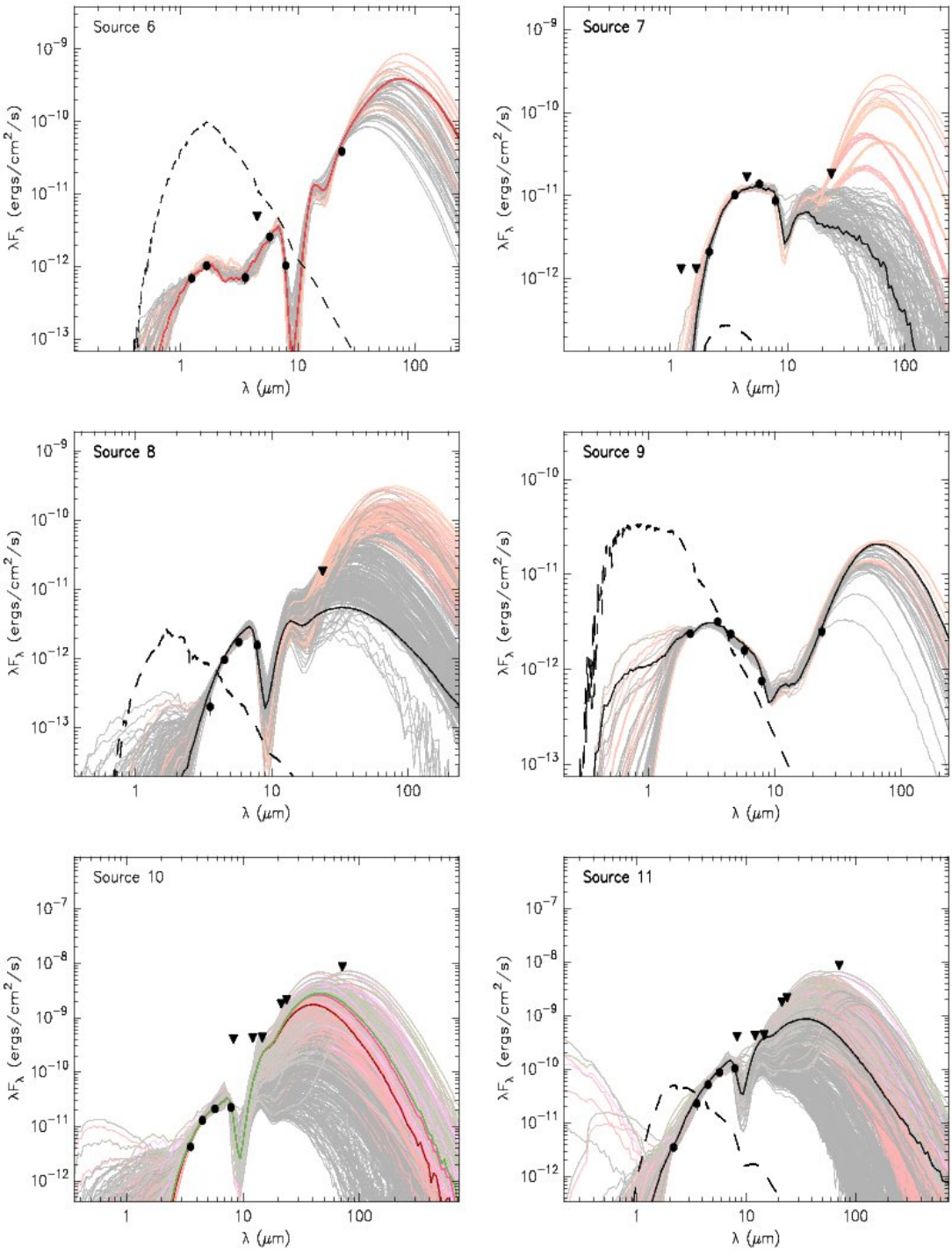
Source 6
Source 7
Source 8
Source 9
Source 10
Source 11
λF_λ (ergs/cm²/s)
λ (μm)

Figure 12a.

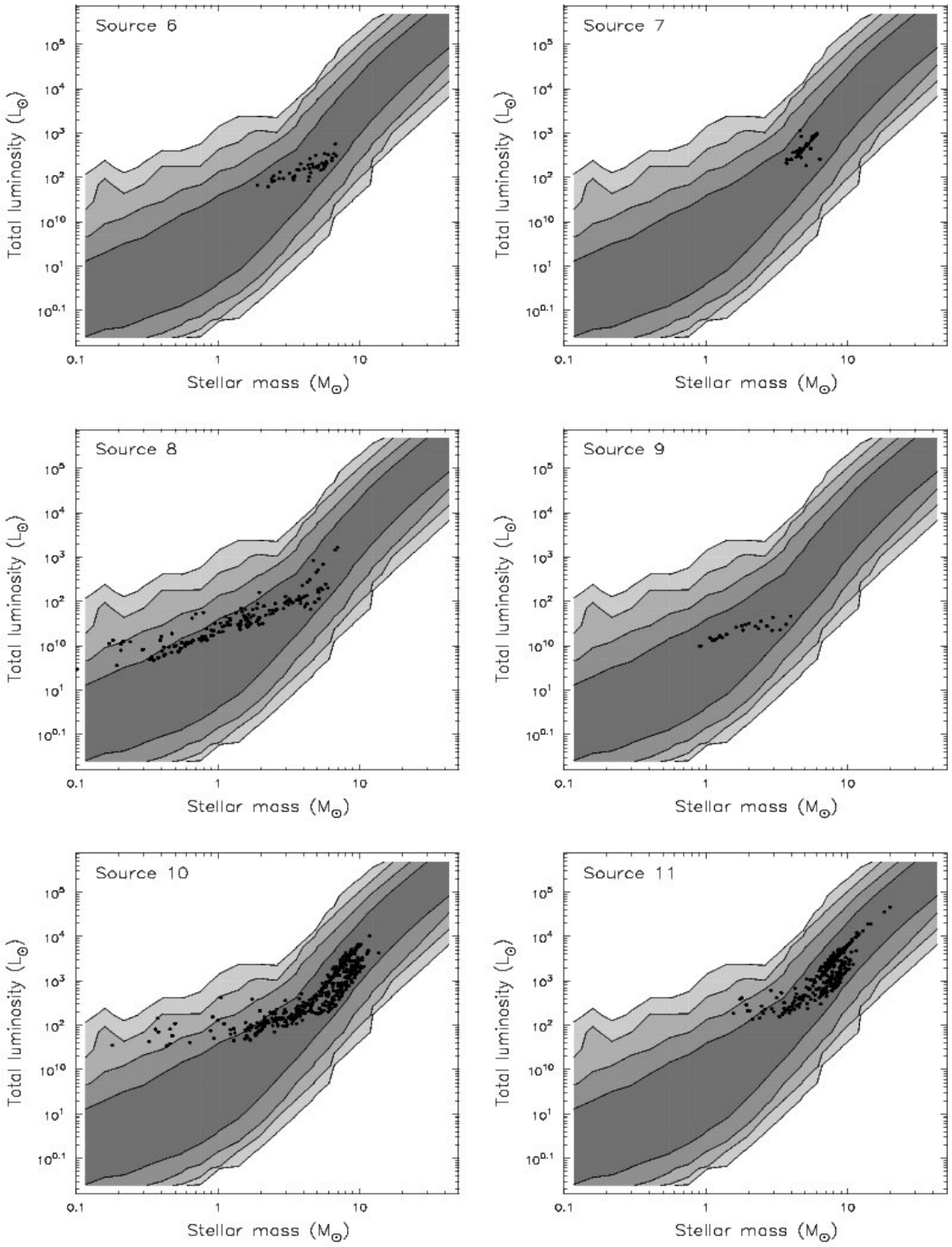
Source 6
Source 7
Source 8
Source 9
Source 10
Source 11
Total luminosity (L⊙)
Stellar mass (M⊙)
0.1
1
10

Figure 12b.